

NO-A189 023

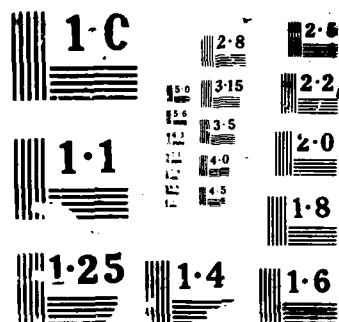
EDDY CURRENT NONDESTRUCTIVE INSPECTION OF GRAPHITE
EPOXY USING FERRITE CUP CORE PROBES(U) NAVAL SURFACE
WARFARE CENTER SILVER SPRING MD 5 N VERNON SEP 87
NSWC-TR-87-149 F/G 11/4

1/1

UNCLASSIFIED

F/G 11/4

ML



4

NSWC TR 87-148

DTIC FILE COPY

AD-A189 823

EDDY CURRENT NONDESTRUCTIVE INSPECTION OF GRAPHITE EPOXY USING FERRITE CUP CORE PROBES

BY SUSAN N. VERNON

RESEARCH AND TECHNOLOGY DEPARTMENT

SEPTEMBER 1987

Approved for public release; distribution is unlimited.

DTIC
ELECTE
JAN 25 1988
S H D



NAVAL SURFACE WARFARE CENTER

Dahlgren, Virginia 22448-5000 • Silver Spring, Maryland 20903-5000

88 1 14 086

UNCLASSIFIED

SECURITY CLASSIFICATION OF THIS PAGE

REPORT DOCUMENTATION PAGE

1a REPORT SECURITY CLASSIFICATION UNCLASSIFIED			1b RESTRICTIVE MARKINGS		
2a SECURITY CLASSIFICATION AUTHORITY			3 DISTRIBUTION AVAILABILITY OF REPORT Approved for public release; distribution is unlimited.		
2b DECLASSIFICATION/DOWNGRADING SCHEDULE					
4 PERFORMING ORGANIZATION REPORT NUMBER(S) NSWC TR 87-148			5 MONITORING ORGANIZATION REPORT NUMBER(S)		
6a NAME OF PERFORMING ORGANIZATION Naval Surface Warfare Center		6b OFFICE SYMBOL (If applicable) R34		7a NAME OF MONITORING ORGANIZATION	
6c ADDRESS (City, State, and ZIP Code) 10901 New Hampshire Avenue Silver Spring, MD 20903-5000			7b ADDRESS (City, State, and ZIP Code)		
8a NAME OF FUNDING SPONSORING ORGANIZATION		8b OFFICE SYMBOL (If applicable)		9 PROCUREMENT INSTRUMENT IDENTIFICATION NUMBER	
8c ADDRESS (City, State, and ZIP Code)		10 SOURCE OF FUNDING NUMBERS			
		PROGRAM ELEMENT NO 62234N		PROJECT NO TASK NO WORK UNIT ACCESSION NO 1280316705	
11 TITLE (Include Security Classification) Eddy Current Nondestructive Inspection of Graphite Epoxy Using Ferrite Cup Core Probes					
12 PERSONAL AUTHOR(S) Susan N. Vernon					
13a TYPE OF REPORT Final		13b TIME COVERED FROM _____ TO _____		14 DATE OF REPORT (Year, Month, Day) 1987, September	
15 PAGE COUNT 72					
16 SUPPLEMENTARY NOTATION					
17 COSATI CODES			18 SUBJECT TERMS (Continue on reverse if necessary and identify by block number)		
FIELD	GROUP	SUB GROUP			
14	02		Nondestructive Inspection		
11	02	01	Eddy Current		
			Composite Materials		
19 ABSTRACT (Continue on reverse if necessary and identify by block number) This report summarizes the results of a three-year project to develop the eddy current technical base for the detection and measurement of broken-fiber damage in graphite epoxy using eddy current. Since graphite epoxy components are frequently made of panels having only one accessible surface, a single-sided technique using a probe coil was required. Parameters of ferrite pot core probes which affect the defect sensitivity of the probe were identified and evaluated in terms of the coil efficiency factor or coupling coefficient. As a result of this investigation, it is possible to optimize eddy current probes for the single-sided inspection of graphite epoxy and other high resistivity materials. Empirical models were developed to estimate the thickness of undamaged material between the scanned surface and the damage to within $\pm 10\%$ and to measure material resistivity to within $\pm 10\%$.					
20 DISTRIBUTION AVAILABILITY OF ABSTRACT <input checked="" type="checkbox"/> UNCLASSIFIED UNLIMITED <input type="checkbox"/> SAME AS RPT <input type="checkbox"/> DTIC USERS			21 ABSTRACT SECURITY CLASSIFICATION UNCLASSIFIED		
22a NAME OF RESPONSIBLE INDIVIDUAL Susan N. Vernon			22b TELEPHONE (Include Area Code) (202) 394-1029		22c OFFICE SYMBOL R34

DD FORM 1473, 84 MAR

83 APR edition may be used until exhausted
All other editions are obsolete

SECURITY CLASSIFICATION OF THIS PAGE

★ U.S. Government Printing Office: 1985-539-012

0102-LF-014-6602

i



UNCLASSIFIED

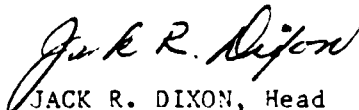
A-1

FOREWORD

This report summarizes the results of a three-year project to develop the eddy current technical base for detection and measurement of broken-fiber damage in graphite epoxy using eddy current. Since graphite epoxy components are frequently made of panels having only one accessible surface, a single-sided technique using a probe coil was required. Parameters of ferrite pot core probes which affect the defect sensitivity of the probe were identified and evaluated in terms of the coil efficiency factor or coupling coefficient. As a result of this investigation it is possible to optimize eddy current probes for the single-sided inspection of graphite epoxy and other high resistivity materials. Empirical models were developed to estimate the thickness of undamaged material between the scanned surface and the damage to within $\pm 10\%$ and to measure material resistivity to within $\pm 10\%$.

This project was funded as part of the Office of Naval Technology-sponsored Ship and Submarine Materials Block (ND2B), managed by Mr. I. Caplan of the David Taylor Research Center (DTRC 0115). The effort was supervised by Mr. Clifford W. Anderson, R34, Naval Surface Warfare Center. The program element is PE62234N. This report satisfies a milestone under work unit number 1280316705.

Approved by:


JACK R. DIXON, Head
Materials Division

CONTENTS

<u>Chapter</u>		<u>Page</u>
1	INTRODUCTION.....	1
	BACKGROUND.....	1
	ADVANTAGES OF EDDY CURRENT.....	2
	TECHNICAL ISSUES.....	3
	APPROACH.....	5
2	IMPEDANCE DIAGRAM ANALYSIS.....	7
3	COUPLING.....	14
	SIGNIFICANCE.....	14
	DESCRIPTION.....	14
	FACTORS AFFECTING THE COUPLING COEFFICIENT.....	16
	COUPLING COEFFICIENT AS A MEASURE OF QUALITY.....	17
4	RESISTIVITY MEASUREMENT.....	23
	INTRODUCTION.....	23
	RESISTIVITY MODEL.....	23
	THICKNESS EFFECTS.....	27
	APPLICATION TO GRAPHITE EPOXY.....	30
	EDDY CURRENT CONDUCTION IN GRAPHITE EPOXY.....	33
5	DETECTION AND MEASUREMENT.....	36
	INTRODUCTION.....	36
	PROBE SIZE AND FREQUENCY.....	36
	DETECTION AND AREA MEASUREMENT.....	37
	DEPTH MEASUREMENT.....	42
	ERROR ANALYSIS.....	46
6	DISCUSSION AND SUMMARY.....	49
	AREAS REQUIRING FURTHER ATTENTION.....	49
	DISCUSSION.....	50
	SUMMARY.....	50
	REFERENCES.....	52
	NOMENCLATURE.....	55
APPENDIX		
A	DERIVATION OF RELATIONSHIP BETWEEN THE COUPLING COEFFICIENT AND X_c	A-1
B	ONE-DIMENSIONAL EDDY CURRENT CASE.....	B-1

ILLUSTRATIONS

<u>Figure</u>		<u>Page</u>
1	SCHEMATICS ILLUSTRATING PERTINENT DIMENSIONS OF DAMAGE IN GRAPHITE EPOXY AND IN METAL.....	3
2	IMPEDANCE DIAGRAM.....	8
3	NORMALIZED IMPEDANCE DIAGRAM.....	9
4	THREE SURFACE PROBE CONFIGURATIONS.....	10
5	NORMALIZED IMPEDANCE DIAGRAMS OF FOUR TYPICAL FERRITE CUP CORE PROBES.....	11
6	FULLY NORMALIZED (K=1) IMPEDANCE DIAGRAMS OF FOUR FERRITE CUP CORE PROBES.....	13
7	EFFECT OF COUPLING ON DEFECT RESPONSE.....	15
8	EFFECT OF SHIELDING LOWER PORTION OF IMPEDANCE DIAGRAM.....	18
9	EFFECT OF SHIELDING AT MID-RANGE OF IMPEDANCE DIAGRAM.....	18
10	SIMILARITIES BETWEEN IMPOSED AND INTRINSIC SHIELDING.....	19
11	EFFECT OF SHIELDING ON DEFECT RESPONSE.....	20
12	LIFT OFF ANGLE α VERSUS X_{nn}	22
13	$TAN \theta_L$ VERSUS r/δ FOR FERRITE CUP CORE - 3-DIMENSIONAL CASE... 24	24
14	a. THREE-DIMENSIONAL FIELD (X,Y, AND Z), b. ONE-DIMENSIONAL FIELD (Z), c. TWO-DIMENSIONAL FIELD (X,Y).....	25
15	$TAN \theta_L$ VERSUS r/δ FOR 1-, 2-, AND 3-DIMENSIONAL CASES.....	26
16	APPROXIMATION OF THICKNESS LOCI.....	28
17	$TAN \theta_E/TAN \theta_P$ VERSUS T/δ	29
18	ρ_P AND ρ_E VERSUS FREQUENCY FOR ALUMINUM.....	31
19	ρ_P AND ρ_E VERSUS FREQUENCY FOR CARBON/CARBON.....	31
20	ρ_P AND ρ_E VERSUS FREQUENCY FOR PAN FIBER SATIN WEAVE GRAPHITE EPOXY.....	32
21	ρ_P AND ρ_E VERSUS FREQUENCY FOR PITCH BASED GRAPHITE EPOXY....	33
22	ρ_P AND ρ_E VERSUS FREQUENCY FOR PAN FIBER GRAPHITE EPOXY.....	34
23	SCHEMATIC OF EDDY CURRENT C-SCAN SYSTEM.....	37
24	RELATIONSHIPS BETWEEN O-COMPONENT OF DEFECT RESPONSE AND r/δ ..	38
25	EDDY CURRENT (a) AND ULTRASONIC (b) C-SCANS OF AN IMPACT DAMAGED GRAPHITE EPOXY PANEL.....	39
26	ULTRASOUND (UPPER) AND EDDY CURRENT (LOWER) C-SCANS SHOWING DAMAGE IN A FILAMENT WOUND CYLINDER HAVING A 0.6 INCH (15.2mm) THICK WALL.....	40
27	EDDY CURRENT AND ULTRASONIC C-SCANS OF IMPACT DAMAGED PANEL WITH HONEYCOMB BACKING.....	41
28	EFFECT OF DEFECT DEPTH ON DEFECT RESPONSE.....	43
29	NORMALIZED DEFECT PHASE ANGLE VERSUS \sqrt{ar}/δ FOR METALS AND A CARBON/CARBON.....	45
30	NORMALIZED DEFECT PHASE ANGLE VERSUS \sqrt{ar}/δ FOR SATIN WEAVE GRAPHITE EPOXY.....	47
31	NORMALIZED DEFECT PHASE ANGLE VERSUS \sqrt{ar}/δ FOR PITCH-BASED FIBER TAPE MATERIAL AND FOR PAN FIBER TAPE MATERIAL.....	47

ILLUSTRATIONS (cont.)

32	PERCENT ERROR IN a VERSUS \sqrt{ar}/δ	48
A-1	COUPLED CIRCUIT DIAGRAM.....	A-1
B-1	SCHEMATIC OF ONE-DIMENSIONAL FIELD.....	B-2

CHAPTER 1

INTRODUCTION

BACKGROUND

In March 1861 the Civil War Battle between the MONITOR and the MERRIMAC marked the beginning of the end of the Navy's reliance on nature's most useful composite material-wood. This traditional structural material was replaced first by iron, then later high strength steel and aluminum alloys with their higher strength to weight ratios and greater damage tolerances. The recent around-the-world flight of the Voyager has been heralded as the beginning of the age of advanced composites. These new, manmade composites such as graphite epoxy offer still higher strength to weight ratios as well as greater damage tolerance.

The Navy has recognized these advantages and is utilizing graphite epoxy to an increasing extent, particularly in aircraft. The material has considerable potential for submersibles as well, since the material has the potential of providing both strength and stealth. As problems in the fabrication of thick-wall structures are solved, use of graphite epoxy and other advanced composites may become as common in the fleet as steel and aluminum are today.

The level of today's advanced composite technology is not unlike that of metallurgical engineering in the earlier part of this century. Since the material failure mechanisms were not understood, large safety margins were provided in the design; a hairline crack in the metal wing of an early WWII fighter plane was not a matter for concern. Since the limits of performance, and thus the power-to-weight, are important, such large safety margins can no longer be afforded. A similar crack in today's metal aircraft wing designed to very close tolerances could result in disaster.

When the failure mechanisms of graphite epoxy are better understood, components and structures of this material may also be more closely designed. The nondestructive inspection (NDI) technology must be available to detect that invisible or barely visible damage. Such NDI technology is also a vital tool during the materials development stage. It has the potential to determine the condition of virgin material as part of the process of optimizing fabrication techniques. If used during fatigue testing, it can monitor the onset and growth of damage. Thus, the safe and economical utilization of graphite epoxy structures in the fleet as well as the maximum utilization of the unique properties of the material requires a nondestructive technology that will effectively inspect the material.

Besides its higher strength-to-weight ratio, graphite epoxy differs from metals with respect to a number of characteristics. Composite materials are, by definition, inhomogeneous. Natural inhomogeneities may mask unacceptable deviations from normal material. Fabrication-related defects such as weak or nonexistent

interlaminar bonding as well as variations in fiber density and twisted fiber tows can weaken the material and need to be detected.

The nature of the damage sustained by graphite epoxy is also different from the well-defined pits and cracks that are typically of interest in metals. Service-incurred damage most commonly results from impact. Impact damage consists of poorly defined regions containing varying densities of delamination and broken fibers. Slight damage consists only of delamination, but when the source of the damage is such as to cause more extensive delamination, fiber breakage also occurs.¹

The effects of these various deviations from normal on the strength of the material are being currently investigated at a number of facilities. As mentioned above these investigations are facilitated by the use of NDI. Once the design engineers have defined the acceptance level for each type of abnormality, NDI techniques must be available to detect and quantify them.

Techniques most commonly used in the NDI of graphite epoxy include visual inspection, the tap test, radiography, and ultrasonics.^{2,3} Visual inspection is, of course, limited to surface defects. Even impact damage is often subsurface or visible only on the back, and frequently inaccessible, surface. The tap test provides a response which varies with material and structure, requires expertise, is highly subjective, and does not provide quantitative information. Low energy radiography can pinpoint localized variations in fiber density in relatively thin components. Except in cases where longitudinal exposures are appropriate, the injection of a radio-opaque material is required for the detection of delamination. (Then, of course, the defect must already have been detected by other means and must open to the surface.) Radiography also requires experienced inspectors and is accompanied by the concerns and precautions attendant with the use of all ionizing radiation. Ultrasonics is probably the most widely used technology in the NDI of graphite epoxy. It primarily detects delamination though some investigators have detected broken fibers using back scattering techniques under laboratory conditions.⁴

Until recently the eddy current inspection of graphite epoxy had received very little attention. In the mid 1970s, several investigators (see references 5 through 10) reported the use of eddy current to detect surface defects, lay-up order, and volume fraction. In the last few years, private industry has become interested in the application of eddy current NDI to graphite epoxy.

ADVANTAGES OF EDDY CURRENT

Graphite epoxy is not generally considered to be an electrical conductor; however, the fibers are conducting so the material is amenable to inspection by a properly optimized eddy current system. Since it is the fibers which carry the current, it is their breakage which can be detected. When a component is under tension, it is also the fibers which carry the load. Consequently, damage detected by eddy current directly affects the tensile strength of the material.^{1,11} In contrast, ultrasonic techniques tend to be far more sensitive to delamination than to broken fibers and the compressive strength of a component is affected more by delamination than by broken fibers. Whether both eddy current and ultrasonics, or either one alone, would be used to inspect a particular component should depend on the load-bearing requirements of the component.

As mentioned above, delamination usually occurs prior to fiber breakage. Loss of compressive strength depends on the severity of the delamination, but ultrasound detects even the slightest delamination without regard to its severity. A component could have many regions containing minor and perhaps insignificant delamination, but appear to be highly damaged based on ultrasound indications. Subsequent inspection by eddy current would provide identification of those regions where the delamination was sufficiently severe to result in broken-fiber damage. Eddy current and ultrasonics can be highly complementary in the inspection of graphite epoxy.

TECHNICAL ISSUES

Two characteristics of graphite epoxy require that standard eddy current systems and techniques, designed for the NDI of metals, be modified for graphite epoxy. First there is the problem of its electrical resistivity. The bulk electrical resistivity of the material is not only very high, typically between about 2000 and 20,000 $\mu\Omega\text{cm}$ (several orders of magnitude greater than that of most metals), but studies^{12,13} have shown that the resistivity can be highly frequency dependent between about 0.25 MHz and 50 MHz. It may vary by as much as a hundred percent over this range.

Not only is the resistivity and its behavior different from that of metals, but the damage sustained by graphite epoxy is also very different. It does not consist of well-defined pits or cracks, but rather a combination of delamination and broken fibers.

The schematics in Figure 1 illustrate the differences in the dimensions of the damage that are of interest in the NDI of metals and of graphite epoxy. Since the term "depth" can have various interpretations, the schematics also serve to define the term as it is used in this report. Usually surface breaking cracks are of primary interest in the NDI of metals. (Although, in some cases the more complex corrosion is also of interest.) Important crack dimensions are length and depth, \underline{d} . Since the thickness of the material is usually known, either the dimension \underline{a} or \underline{d} can be measured.

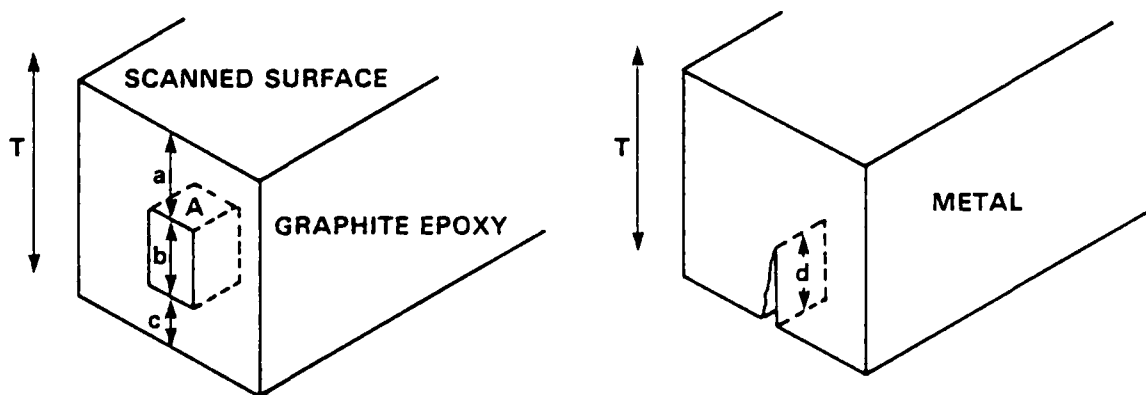


FIGURE 1. SCHEMATICS ILLUSTRATING PERTINENT DIMENSIONS OF DAMAGE IN GRAPHITE EPOXY AND IN METAL

In contrast, in graphite epoxy the damage has an irregularly shaped volume (shown as a cube in the figure) which may break either surface (\underline{a} or $\underline{b} = 0$), neither surface, or both surfaces ($\underline{a} = \underline{b} = 0$). Ideally we would like to measure the through-thickness dimension (\underline{d} in the figure), its through-thickness location (\underline{a} and \underline{b}), and its area (\underline{A}). Measuring all three through-thickness dimensions, \underline{a} , \underline{b} , and \underline{d} , is a challenge to any NDI technique and was beyond the scope of this project. Since the dimension \underline{a} , the distance between the accessible surface and the damage, is a factor in repair and is also a significant determinant of component strength, a method was developed for measuring this dimension. Since it refers to the depth at which the damage is located, the dimension \underline{a} is defined as the "depth" in this report.

The high resistivity has three implications for eddy current. First, since the depth to which eddy currents penetrate is proportional to the resistivity of the material, much greater material thicknesses can be examined than are usually associated with eddy current inspection. For example, when the resistivity is $10,000 \mu\Omega\text{cm}$, the depth at which the current density is $1/e$ of the density at the surface (one skin depth or standard depth of penetration) is almost two inches (5.1 cm) at a frequency of 10 kHz.

Second, when the material is relatively thin as are aircraft wing skins, frequencies higher than those usually used in the inspection of metals are required. Ideally the skin depth should be slightly greater than the thickness of the material. When the material is 0.125-inch (3.17 mm) thick and the resistivity is $10,000 \mu\Omega\text{cm}$, then a frequency of 2.5 MHz should be used. Most commercial eddy current instruments were designed for use at lower frequencies for the inspection of metals. At frequencies above about 500 kHz, the phase detector output of these instruments is inaccurate. (This could be addressed with a design appropriate to higher frequencies.)

Finally, larger probes are required for materials having high resistivities (Chapter 5). Standard off-the-shelf eddy current probes were designed for use on metals and are too small. Regardless of its quality or coupling coefficient (Chapter 3), a probe that is too small provides almost no response to graphite epoxy; a small probe does not "see" the material.

Depth measurement requires knowledge of the material resistivity. The variation in the resistivity, both with frequency and among apparently similar materials, means that a method to measure resistivity must be incorporated in an eddy current system to be used in the NDI of graphite epoxy. This is not a requirement in the eddy current NDI of metals. Because of the combination of high resistivity, and too low an upper limit to the frequency range of many commercial impedance analyzers and eddy current instruments, it is not always possible to measure the resistivity at frequencies such that the skin depth is less than the thickness of the material. When the thickness is less than the skin depth, the eddy current response is affected so potential thickness effects must be incorporated in a resistivity model (Chapter 4).

The nature of the damage sustained by graphite epoxy imposes still further requirements on the eddy current system. Regardless of the nature of the damage, it must be detected and its depth should be measured. Defect detectability puts both upper and lower limits on the size of the probe relative to the skin depth as does the requirement to measure the depth of the damage (Chapter 5). The detection

capability of a probe relative to its size also depends on its coupling efficiency (Chapter 3). These restrictions on probe size apply to metals as well as to graphite epoxy, although the ranges of probe sizes are usually different.

An effective means of measuring the planar extent or area of damage in graphite epoxy is the generation of a map of the damaged region. Such a map is generated by raster scanning the probe across the surface of the material and recording the impedance changes (Chapter 5). The accuracy of this map, (or "C-scan" because of its similarity to an ultrasonic C-scan) depends on the resolving power of the probe. Only an infinitely small probe would provide an ideal C-scan, but at least, the smallest and most efficient probe, within the limitations imposed by detection requirements, should be used.

There are a number of excellent sources on the theory of eddy current inspection^{13,14,15} which will not be discussed in-depth here. Suffice it to say that all the information about the test material and its defects is based on interpretations of their effects on the probe impedance. Probe impedance is determined not only by the resistivity of the test material and its geometry and defects, but also by the test frequency and the probe design. The effects of all these factors are best illustrated by the normalized impedance diagram, discussed in the following chapter. Probe sensitivity is discussed in Chapter 3. Resistivity measurement is discussed in Chapter 4, while methods of defect detection and measurement are presented in Chapter 5. Areas requiring further attention, and the discussion and summary, are included in Chapter 6.

APPROACH

The technical issues required a two-pronged approach to the development of an eddy current system to inspect graphite epoxy. System optimization was required to maximize meaningful signals, and models were required to interpret the signals. It was found that the phase detectors on some commercial eddy current instruments were inaccurate at frequencies above about 500 kHz. The instrument-related frequency bias in the data was eliminated by the use of a commercial impedance analyzer. The lower gain provided by the impedance analyzer was compensated for, to the extent possible, by maximizing probe sensitivity. This required development of a criterion to measure probe sensitivity or quality.

A model was required to measure defect depth. Since the eddy current response to a defect depends on the resistivity of the material, a model to measure resistivity was also required. An empirically derived model applies to the specific set of conditions under which the model was derived. Using an appropriate set of calibration standards, it is a straight-forward procedure to correlate, for a specific probe, the probe response with material resistivity over a (relatively) small range of resistivity values, or to correlate the response with defect depth in a material of known resistivity. The absence of resistivity standards in the range of interest, as well as the lack of uniformity in defect geometry, precluded the narrow approach to model development. The goal was the development of empirical models which were not limited to a specific range of resistivities or defect geometries.

To insure, to the extent possible, that the models were not based on a set of specific conditions whose characteristics might not be readily apparent, the data on

which the models were based were collected over the widest possible conditions. While the NDI of metals was not the object of this investigation, the bulk of the data providing the base for the model development was obtained from metals and from a carbon/carbon composite.

The models were developed and tested with data collected with over 20 probes, nine materials, and in most cases, at least two specimens of each material. The probes were fabricated from ferrite cores having a wide range of permeabilities and supplied by several different vendors. The data presented in the figures were selected to illustrate particular effects such as those due to extremes in resistivity or probe size, or to indicate typical data scatter.

CHAPTER 2

IMPEDANCE DIAGRAM ANALYSIS

The impedance of a coil to which an RF signal has been applied has a real (resistive) and an imaginary (reactive) component. As the frequency is increased the reactance increases (Figure 2) since reactance, X , is the product of the frequency and the inductance. There is also an increase with frequency in the resistive component, R . This increase in resistivity was attributed to losses associated with heat, radiation, and eddy currents in the wire and in the ferrite core (if there is one.) When the coil or probe is placed on (coupled to) a conducting material, the eddy currents induced in the material cause a drop in reactance and an increase in resistance. (Figure 2)

Information about the test material and its defects is gained via analysis of the change in the impedance due to the presence of the material. The value of the probe impedance when it is uncoupled to the material (the probe is in air, far removed from the material) is not important. We are interested only in those changes in the impedance caused by the test material. Consequently, we normalize the impedance of the probe when it is coupled to the material with respect to the impedance of the probe in air:

$$R_n = \frac{R_m - R_o}{X_o} \quad X_n = \frac{X_m}{X_o}$$

where R_n and X_n are the normalized values of the real and imaginary components; R_m and X_m are the components of the probe when it is coupled to the material; R_o and X_o are the uncoupled ("air") values.

The resulting normalized impedance diagram (Figure 3) does not contain unnecessary information about the effects of frequency on the impedance, but rather illustrates the effects of the material on the impedance at different frequencies. The normalized impedance diagram also permits the comparison of different probes with respect to their relative sensitivities. Although many of the same design parameters determine both the impedance of the probe in air and its sensitivity, sensitivity and the uncoupled impedance are independent.

Of the three common types of surface probes, illustrated in Figure 4, the ferrite cup core was found to be the most sensitive. (The cross-sectional view of the ferrite cup core probe shows a gap in the center; such a hole through the center of the cup is often present in transformer pot cores.) Because of this greater sensitivity, it was considered the most suitable for graphite epoxy where probe size was found to be an important factor. While the shapes of the normalized impedance diagrams of air core probes depend on the distribution of the windings,¹⁶ we found that the shapes of the diagrams are essentially the same for probes with ferrite cup cores. This similarity is seen in Figures 5 and 6 where the

MEAN PROBE RADIUS: 0.145 IN
MATERIAL: CARBON/CARBON
RESISTIVITY: $842 \cdot \mu\Omega \text{ CM}$

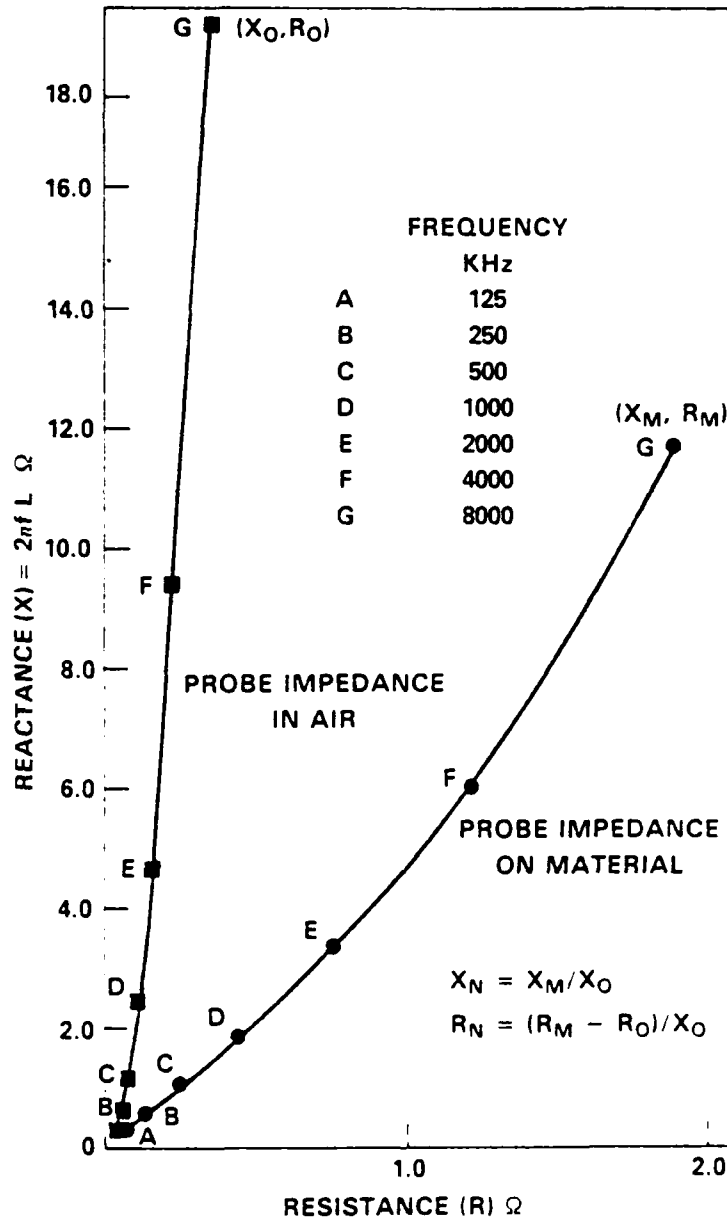


FIGURE 2. IMPEDANCE DIAGRAM

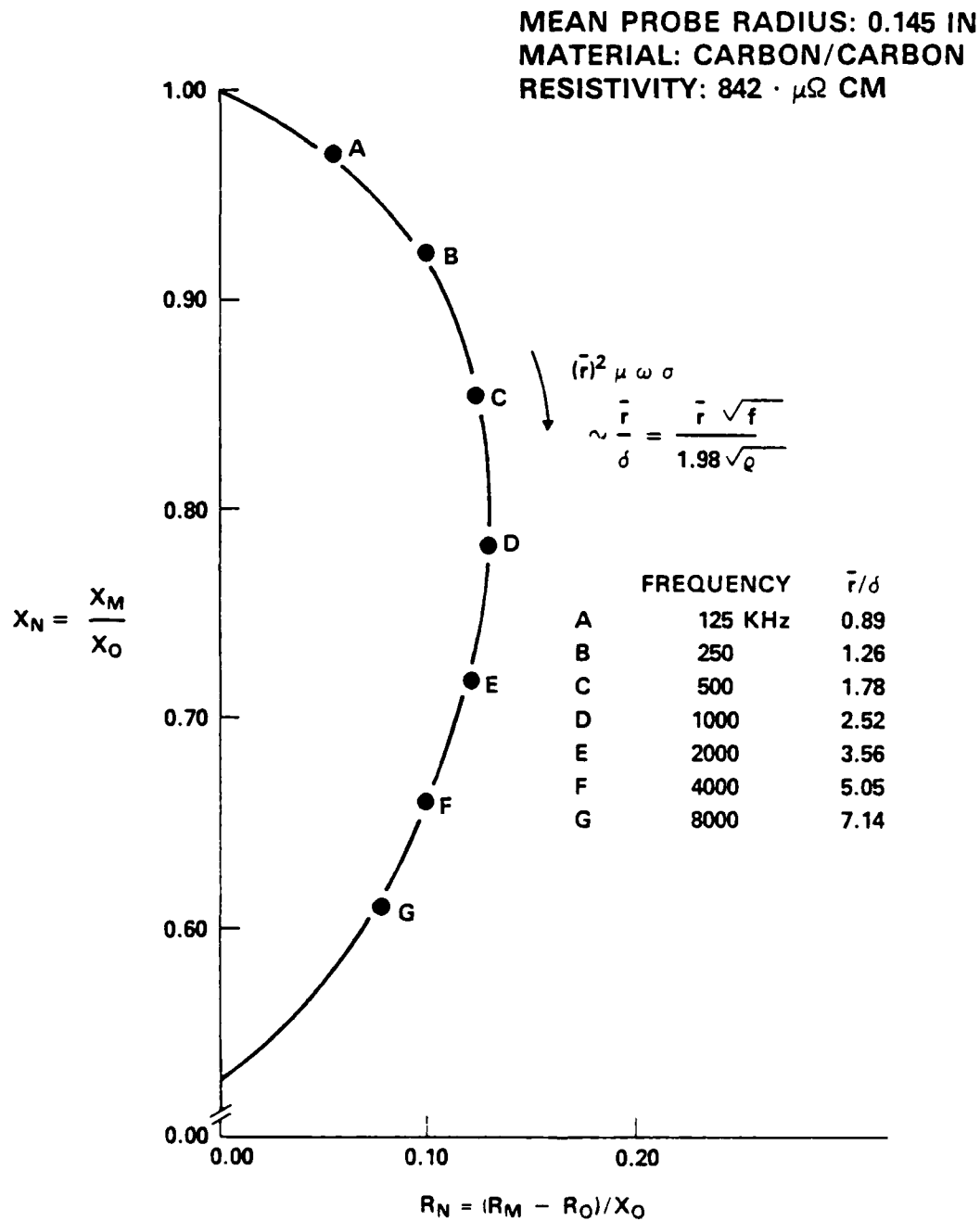


FIGURE 3. NORMALIZED IMPEDANCE DIAGRAM.

 AIR CORE

 FERRITE CYLINDER
CORE

 FERRITE POT (CUP)
CORE

FIGURE 4. THREE SURFACE PROBE CONFIGURATIONS

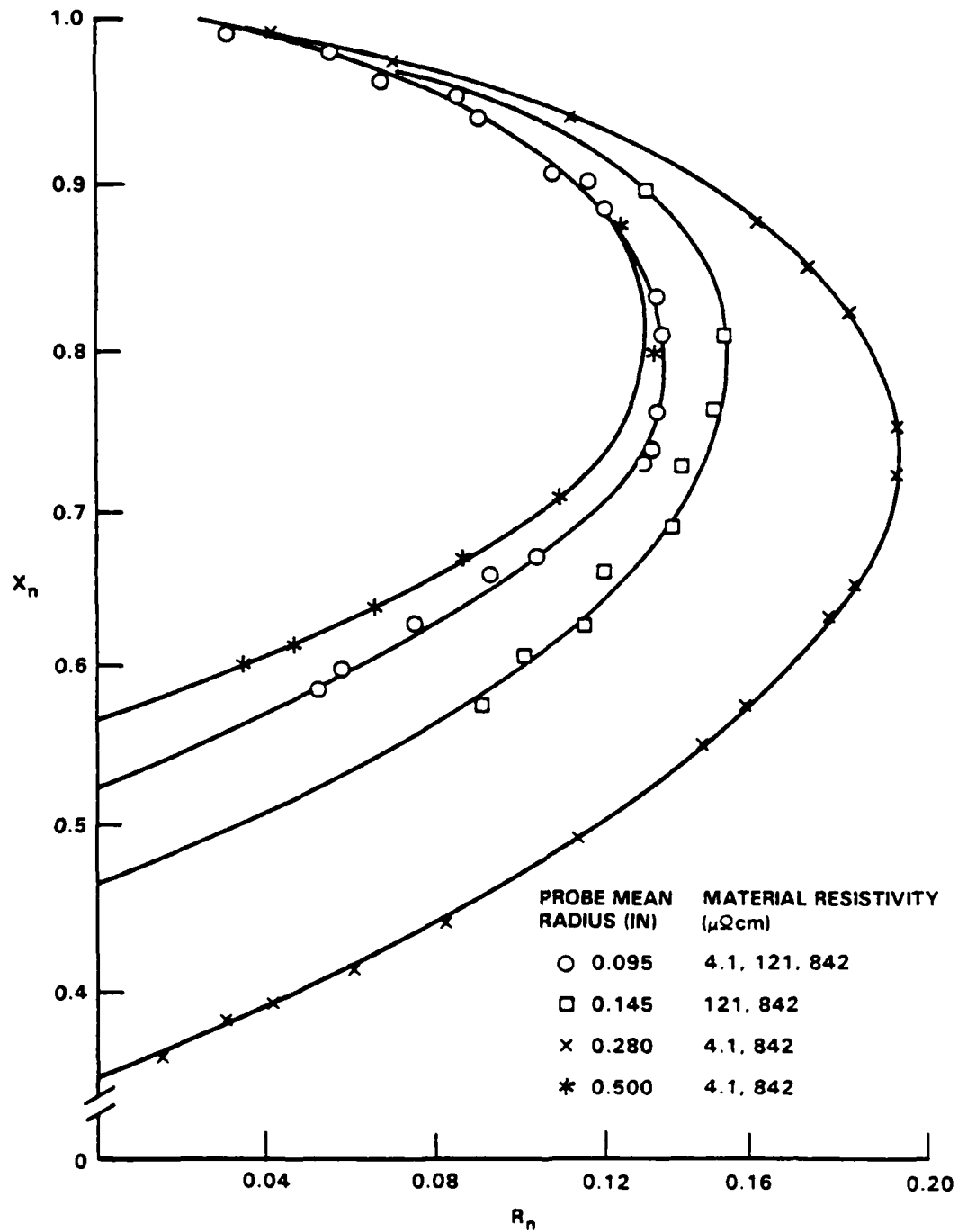


FIGURE 5. NORMALIZED IMPEDANCE DIAGRAMS OF FOUR TYPICAL FERRITE CUP CORE PROBES.

normalized impedance diagrams of four very different, but typical, ferrite cup coreprobes are shown. The sizes (extent in the resistive and reactive directions) of the Figure 5 impedance diagrams differ as a consequence of the different coupling coefficients of the four probes (Chapter 3). However the four diagrams are virtually identical (Figure 6) when further normalized with respect to the intercept, X_c .

$$X_{nn} = \frac{X_n - X_c}{1 - X_c} \quad (1)$$

$$R_{nn} = \frac{R_n}{1 - X_c} \quad (2)$$

where R_{nn} and X_{nn} are the full-scale values of the real and imaginary components and X_c is the point on the imaginary axis where it is intersected by the curve extrapolated to higher conductivity or frequency values. These four ferrite cup core probes differ not only with respect to size but also the ferrite materials which constitute their cores. The impedance diagrams of all the probes investigated fell on this curve when the data were normalized with respect to their respective X_c values. The similarity of the impedance curves for ferrite cup core probes, regardless of other design parameters, facilitates their comparison, evaluation, and the interpretation of their responses to defects.

The impedance diagrams shown in Figures 2 and 3 were generated by placing the probe on a single material and increasing the frequency. Each point on the diagram has associated with it a specific value of the dimensionless ratio, r/δ , where r is the mean coil radius and δ is the skin depth, or standard depth of penetration. In the case of the nonmagnetic materials considered here, skin depth in mm is given by

$$\delta = 50.29 \sqrt{\rho/f}$$

where resistivity, ρ , is in $\mu\Omega\text{cm}$ and frequency, f , is in Hertz.

The same diagrams could have been generated by keeping the frequency constant and using materials of increasing conductivities, or by changing the radius of the probe.

The sensitivity of a probe to defects in the material is related, in large part, to the size of the normalized impedance diagram. Sensitivity can be described by the coupling coefficient of the coil.

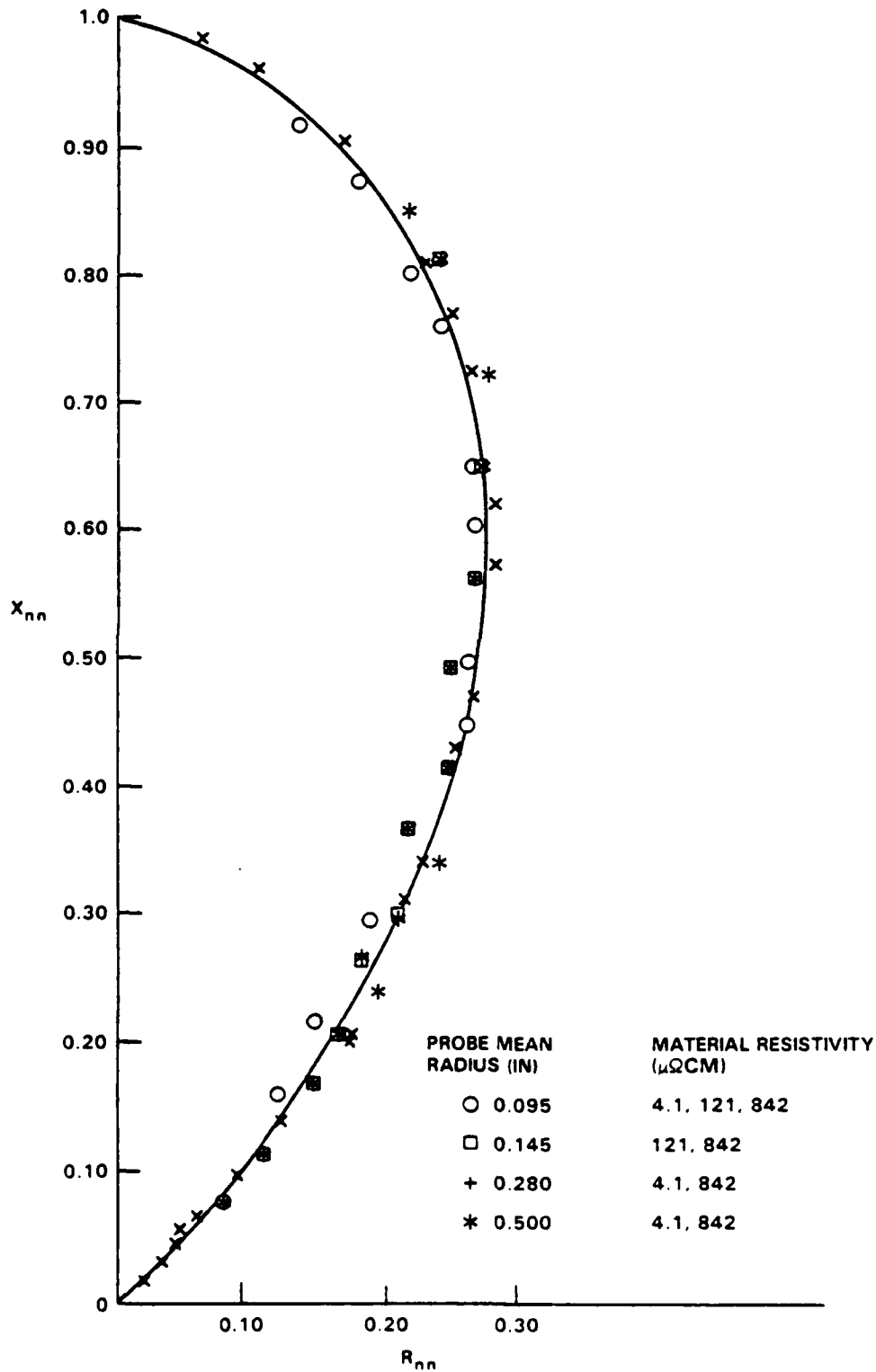


FIGURE 6. FULLY NORMALIZED ($K = 1$) IMPEDANCE DIAGRAMS OF FOUR FERRITE CUP CORE PROBES

CHAPTER 3

COUPLING

SIGNIFICANCE

The importance of good coupling is illustrated in Figure 7. The defect vector represents the change in impedance associated with a particular defect at different points on the diagram. The inner curve was generated with a 0.04-in(1 mm) separation (lift-off) between the probe and the material. The effect of the poorer coupling on the magnitudes of the defect vectors is obvious. In fact, at point A on the inner curve, the defect response was so small it was not repeatable. A probe which couples well to the material is more sensitive to defects. As mentioned in the introduction, it is desirable to use the smallest probe possible consistent with other requirements. If the coupling between the probe and the material is good, a smaller probe can be used to detect a particular defect. In other words, a small sensitive probe may be superior to a larger less sensitive probe.

DESCRIPTION

The coupling between an eddy current probe and the test material can be likened to a two-mesh circuit where the primary circuit is the eddy current probe and the secondary circuit is the test material. The coefficient of coupling between the primary and secondary circuits is equal to that fraction of the total flux associated with the primary circuit which links with the secondary. The coupling coefficient is a measure of the efficiency with which the energy of the coil is transmitted to the test material. Dr. Paul W. Gammel of the Naval Surface Warfare Center has shown (see Appendix A) that the coupling coefficient, K is given by

$$K^2 = 1 - X_c. \quad (3)$$

This coupling coefficient is related to the coil efficiency factor, η , of surface probes^{14,15} since

$$\eta = 1 - X_c.$$

In the case of an encircling coil and conducting cylinder, η is referred to as the fill-factor and is a measure of the extent to which the cylinder (diameter D) fills the encircling coil (diameter d) or

$$\eta = \frac{D^2}{d^2}.$$

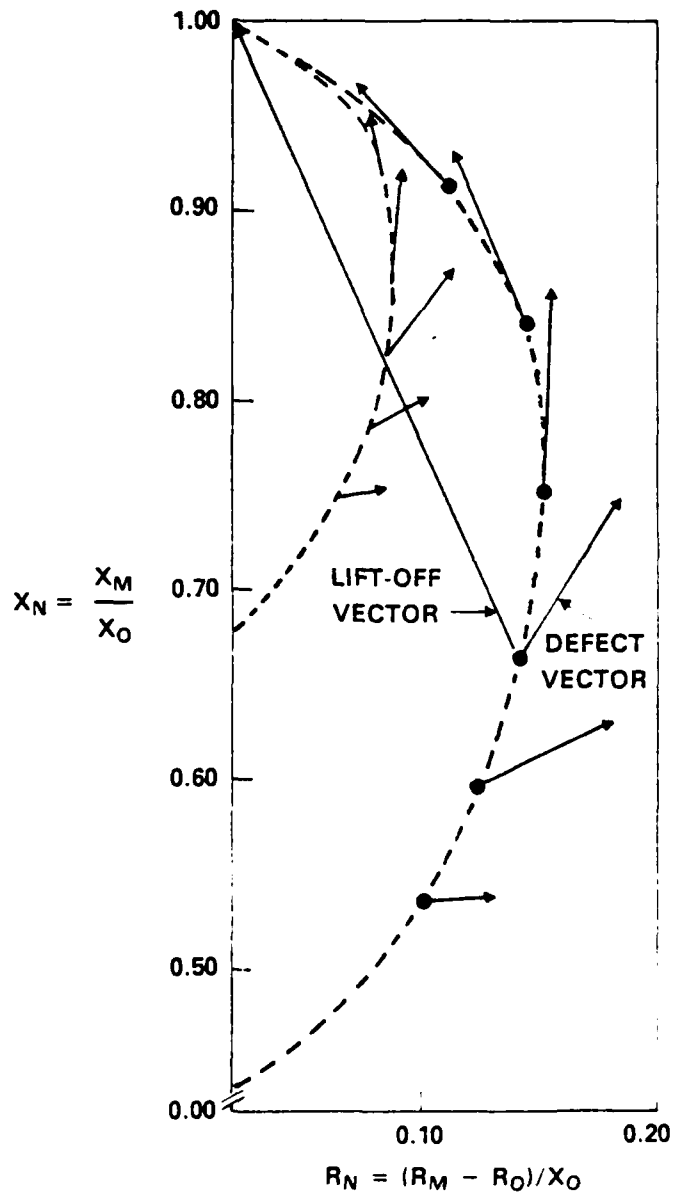


FIGURE 7. EFFECT OF COUPLING ON DEFECT RESPONSE

So in the case of the encircling coil the coupling coefficient is equal to the ratio of the radius of inner cylinder to the radius of the outer coil.

The fill-factor in the case of the encircling coil (or the feed-through coil where the inverse of the above ratio applies) is generally equated to lift-off for a probe coil, where lift-off is the separation between the probe and the material. The negative effect of lift-off on coupling was evident in Figure 7. There are a number of additional factors which affect the coupling coefficient of a ferrite cup core probe.

FACTORS AFFECTING THE COUPLING COEFFICIENT

The most obvious factor affecting the coupling coefficient is the lift-off separation between the probe and the test material. Naturally, the closer the probe is to the material, the more of the probe flux will link with the material.

The second factor is probe type.^{17,18} Early in this investigation, it was found that the coupling provided by ferrite cup core probes has the potential to be far superior to that provided by the air core. The ferrite acts as a shield and concentrates the flux, causing a greater proportion of the flux associated with the coil to link with the material. The magnetic permeability of the ferrite would be expected to have a significant additional effect on coupling, since the higher the permeability the greater the shielding. A systematic investigation of the effects of permeability was beyond the scope of this project. It was observed that the permeability of the ferrite did not affect the shape of the impedance diagram for permeability values between 100 and 3000.

Numerical models have been developed for air core probes.^{19,20} Similar models are being developed for ferrite cup core probes²¹ but as yet these models do not permit determination of the coupling coefficient, nor do they provide correlations between the probe response with material resistivity and defect depth. The greater efficiency of the ferrite cup core warranted the development of empirical models. Hopefully, these models will be substantiated later by theory.

A third factor, the distribution of the windings, has been found to be significant in air core probes.²² The closer the bulk of the windings to the test material, the better the coupling. This was also found to be a factor in ferrite cup core probes. However, another factor was found to be more significant. Coupling was improved if thick wire was used. The improvement in the coupling began to occur at that frequency where the skin depth in the copper wire was about equal to the radius of the wire.²³ This effect is illustrated in Figure 8. The inner curve was generated with a probe wound with ≈ 32 wire, having a radius of 0.008 inch (0.20 mm). The probe which generated the outer curve was wound with ≈ 20 wire having a radius of 0.016 inch (0.41 mm). The change in slope of the impedance curve, indicating an improvement in coupling, occurred at about 16 kHz. At that frequency the skin depth in the wire is 0.021 inch (0.53 mm), or about equal to the radius of the wire. The corresponding frequency for the inner curve was 400 kHz and the highest frequency plotted here was 100 kHz. The expected change in slope at 400 kHz was observed in data where the 400 kHz point fell higher on the curve. Data for other wire sizes showed similar correlations between the wire radius and the frequency at which the coupling began to improve.²³ The data in Figure 8 were generated on aluminum where the location on the normalized impedance diagram of the

improvement in coupling is too low to be useful (see following section). The impedance diagram for the same probe on a carbon/carbon composite having a resistivity of $842 \mu\Omega\text{cm}^{13}$ is included in Figure 9. Here it can be seen that the benefits provided by the thicker wire occur in the upper and useful portion of the diagram.

The frequency at which the change in slope occurred, the critical frequency f_c , depended only on the radius of the wire. The effect occurred if there were only two or three turns of wire of sufficient thickness relative to the frequency and the effect did not occur if the wire were too thin, even if the cup were filled with turns. The change in slope is very similar to the type of change which occurs when a copper foil is placed around the inner surface(s) of the cup.^{23,24} This copper foil shields the inner surfaces of the cup, eliminating some of the flux linkage within the cup, and thereby forcing that flux out of the cup and into the adjacent test material. It is assumed that the wire provides a similar shielding effect when the frequency is sufficiently high that the skin depth in the wire is less than the wire radius. The similarities between the two cases are illustrated in Figure 10. To emphasize the similarities, in the figure only the outer turns of the thick wire are shown as providing the shielding effect. In fact each turn contributes to the effect. In both cases (the imposed copper shielding and the intrinsic wire shielding) the increased flux linkage with the test material results in improved coupling above the critical frequency.

The effects of the improved coupling on defect response magnitude are shown in Figure 11. To generate these data, shielding was added in the form of a 0.005 inch (0.13mm)-thick copper foil placed around the center post of the cup (approximately 355° , to avoid shorted turn effects). The increase in defect response magnitude is clearly the result of shielding since no other changes were made in the coil. It can be seen that the coupling began to improve at 400 kHz where the skin depth in the foil was about equal to its thickness. The poorer coupling below this critical frequency is typical of shielding effects.

Because of their high conductivities metals are generally inspected at lower frequencies than is graphite epoxy (see the following chapter). Eddy current instruments usually require a certain minimum impedance of the probe; a probe to be used at lower frequencies must have more turns to provide that impedance. If the volume in the core is insufficient for the requisite number of turns of thick wire, shielding can be added in the form of copper (or other highly conducting material) in configurations designed to improve shielding.²⁴ Details of various methods of providing imposed shielding as well as the relative virtues of different shielding materials are discussed in detail in reference 24.

It should be noted that when shielding effects are present, the resistivity and depth models do not apply. Shielding apparently modifies the field of the ferrite cup core probe so the impedance diagram is no longer described by the universal curve. While shielding effects enhance the detection capability of a system, it is important to insure they are not present if the models are to be used.

COUPLING COEFFICIENT AS A MEASURE OF QUALITY

There is a requirement for the establishment of accept/reject criteria for eddy current probes.^{25,26} Assuming the probe size and the inspection frequency for

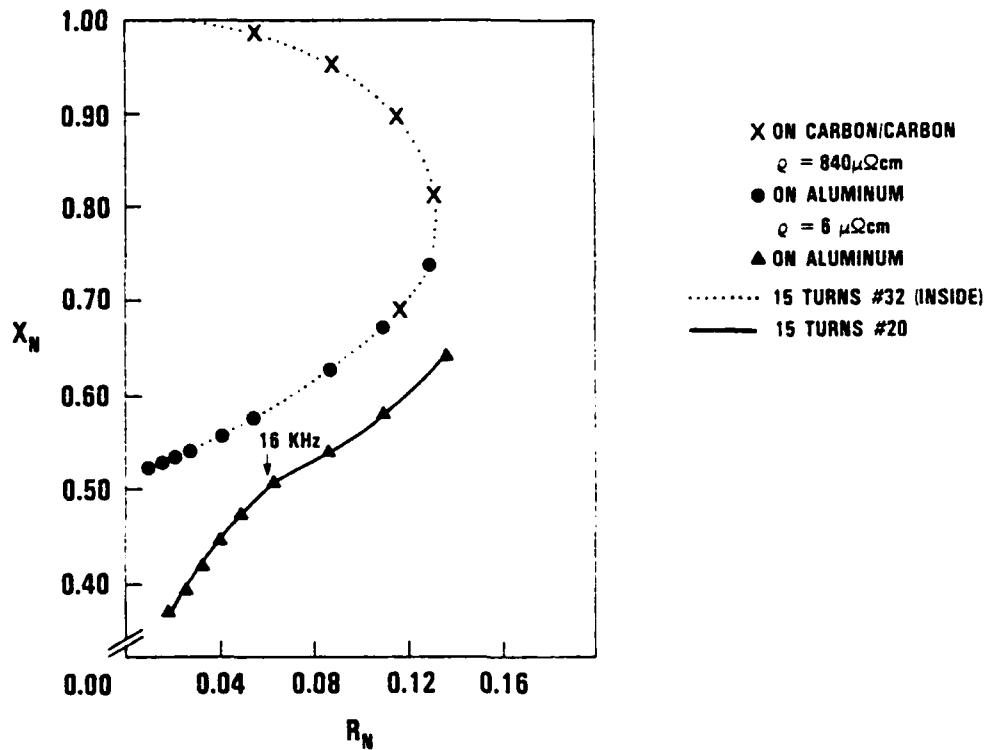


FIGURE 8. EFFECT OF SHIELDING LOWER PORTION OF IMPEDANCE DIAGRAM

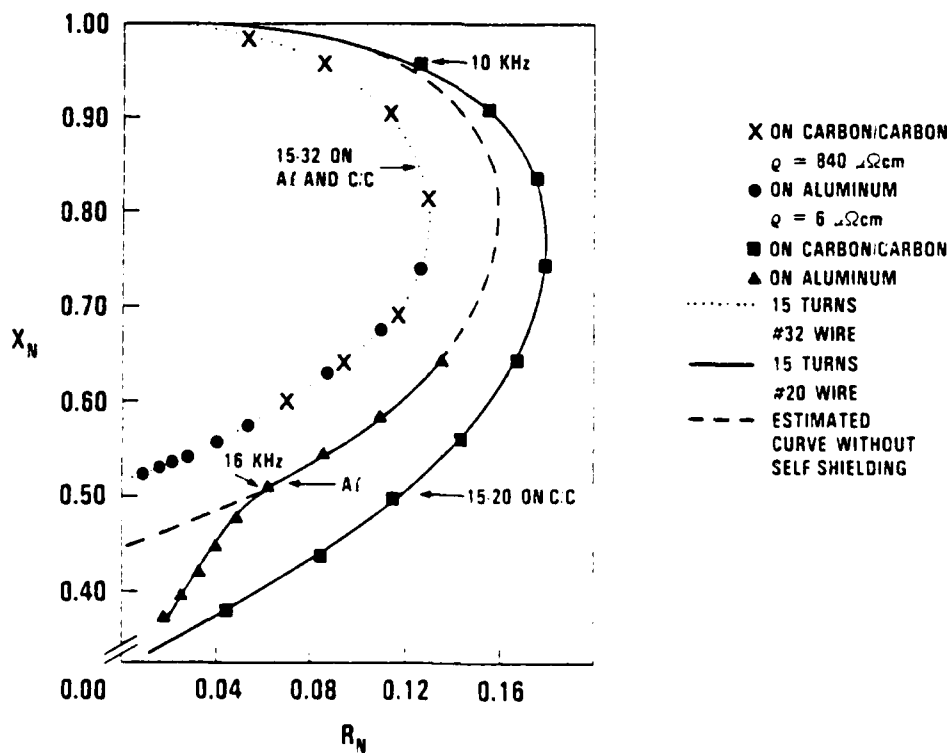


FIGURE 9. EFFECT OF SHIELDING AT MID-RANGE OF IMPEDANCE DIAGRAM

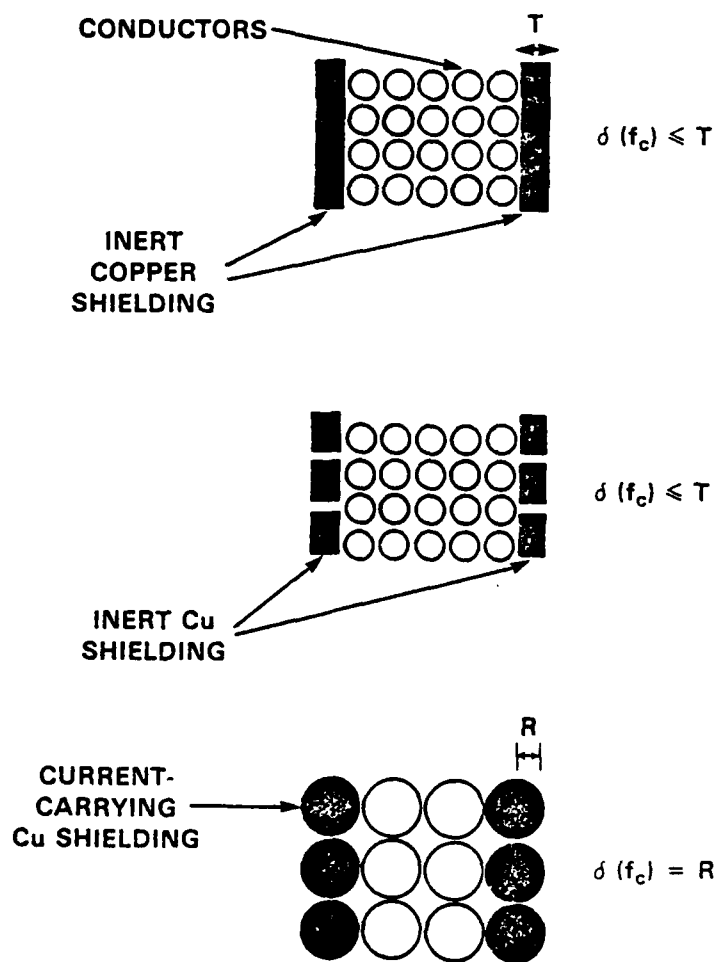


FIGURE 10. SIMILARITIES BETWEEN IMPOSED AND INTRINSIC SHIELDING

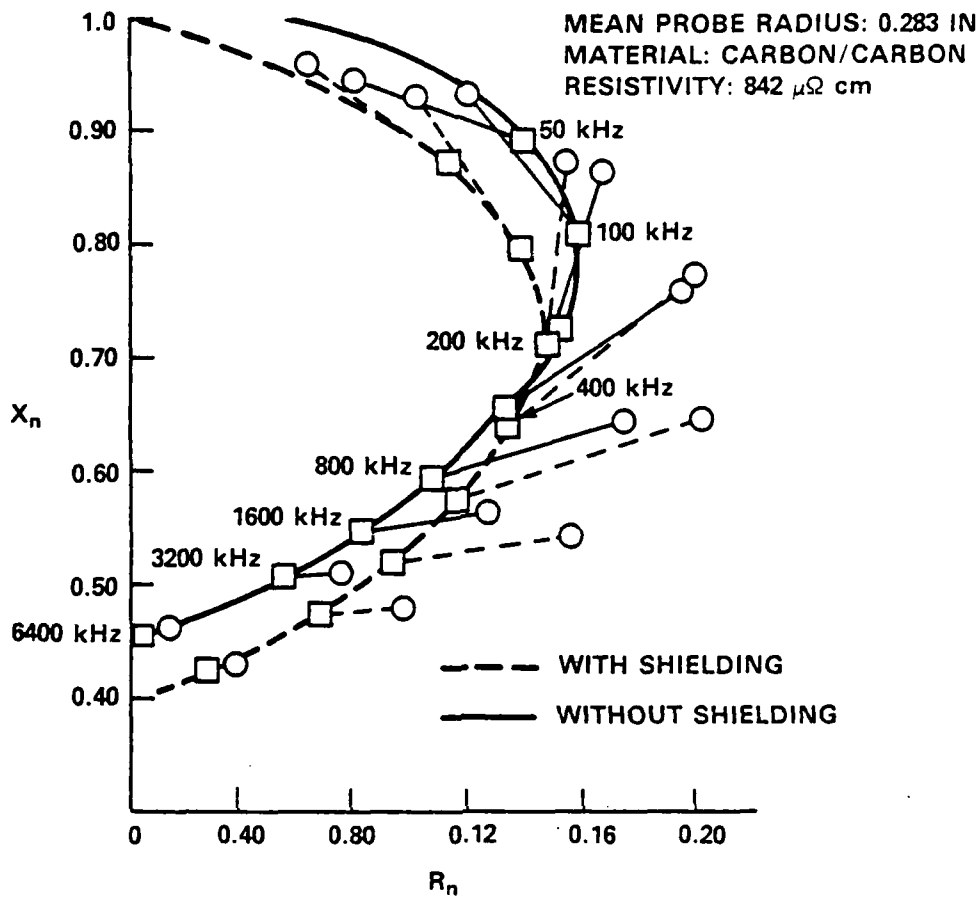


FIGURE 11. EFFECT OF SHIELDING ON DEFECT RESPONSE

frequencies) are appropriate to the material and to the location of the defects (Chapter 5), then the ability of the probe to detect defects depends on its sensitivity, and hence, on its coupling coefficient. The coupling coefficient of a ferrite cup core probe (and possibly other types as well) is thus a measure of its quality. It is a useful measure of quality since its measurement is a simple procedure; no standards or materials of known conductivity are required.

Since $K^2 = 1 - X_c$ (Equation 3), the coupling coefficient can be estimated by extrapolation of the impedance curve to determine X_c , as described above. The values of r/δ associated with each point on the curve do not need to be known to generate the curve, so the resistivity of the material does not need to be known in order to determine the coupling coefficient.

It is also possible to determine the coupling coefficient from a single measurement. By substituting equation 3 into equation 1, it is seen that the coupling coefficient is also given by

$$K^2 = \frac{1 - X_n}{1 - X_{nn}} \cdot \frac{X_{nn}}{X_n} \quad (4)$$

where X_n is the normalized reactance and X_{nn} is the idealized reactance, or the reactance normalized with respect to the coupling coefficient (equations 1 and 2).

Two features of the ferrite cup core probe permit the calculation of X_{nn} , and consequently, the coupling coefficient, via measurement of the normalized impedance at a single point on the curve.

First, the lift-off angle, θ_L , for ferrite cup core probes appears to depend only on the quantity r/δ . The lift-off line, the trace on the impedance plane generated as the distance (lift-off distance) between the probe and material is increased, is generally curved for air core probes.²⁷ The lift-off line can also be determined first by generating a family of impedance curves, each curve generated at a different lift-off separation and then by connecting points having the same r/δ value. It could be seen in Figure 7 that lift-off lines for ferrite cup core probes are straight. If the lines were curved, lift-off angle would depend on the degree of coupling as well as on r/δ . θ_L can be calculated by measuring X_n and R_n and substituting in the trigonometric relationship:

$$\theta_L = \tan^{-1} \frac{1 - X_n}{R_n}.$$

The second important property of the ferrite cup core probe is the apparent universality of the idealized or fully normalized ($K = 1$) impedance diagram shown in Figure 6. This fully normalized impedance diagram, traced out parametrically by r/δ is given by

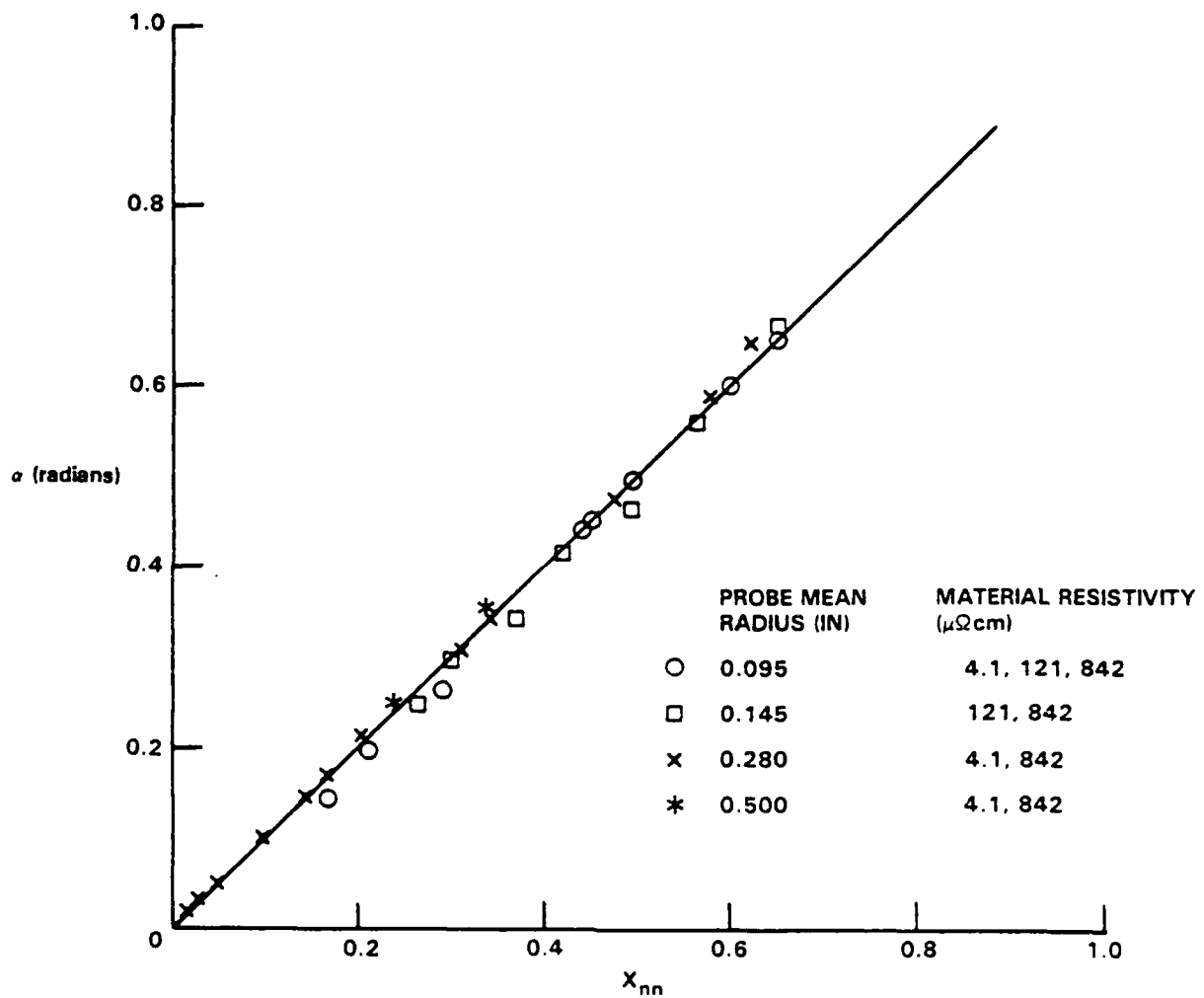
$$\theta_L(r/\delta) = \tan^{-1} \frac{1 - X_{nn}(r/\delta)}{R_{nn}(r/\delta)}. \quad (6)$$

So, while θ_L can be determined from Equation 5, X_{nn} cannot be determined from Equation 6. However, the universal curve exhibited an apparent feature which permits a direct determination of X_{nn} from angle α , the complement of θ_L . It was observed (Figure 12) that the angle α , expressed in radians, is equal to the dimensionless quantity, X_{nn} . The relationship

$$X_{nn} = \alpha(\text{radians})$$

was observed for $\alpha < 45^\circ$ which corresponds to $r/\delta > 1.65$. Scatter in the data in Figure 12 was attributed to errors in the selection of X_c , obtained by visual extrapolation. The theoretical basis for the simplicity of this relationship has not been established, but it facilitates determination of the coupling coefficient. α can be substituted in Equation 4 and the coupling coefficient calculated.

So, to measure the coupling coefficient or quality of a probe, the normalized values of the real and imaginary components, R_n and X_n , are determined; the lift-off angle is calculated; X_n and α are substituted in equation 4. It is not necessary to know anything about the test material except that it is sufficiently thick so that thickness effects are not influencing the response (Chapter 4) and to note that α is less than 45° . Should this angle be greater than 45° , the frequency must be increased appropriately.

FIGURE 12. LIFT-OFF ANGLE α VERSUS X_{nn}

CHAPTER 4

RESISTIVITY MEASUREMENT

INTRODUCTION

The resistivity of the material must be known in order that the defect depth be calculated. Since resistivity is also dependent on the frequency, it must be measured at each frequency used in the depth measurement.

Measurement of the resistivity of graphite epoxy is a significant problem. The insulating epoxy effectively eliminates contact methods. At the present time there are no conductivity meters for the range of interest. There are effective through-transmission²⁸ methods which can be used to measure very high resistivities but these have two drawbacks. Both surfaces of the material must be accessible, and this often is not the case (for example, aircraft wing skins). Also, at the present time through-transmission measurement is possible in the laboratory only; there are no "black boxes" available for field use. The air core model, mentioned earlier, does not apply to the more sensitive ferrite cup core probes. An empirical model was developed to determine resistivity from the responses of these probes.

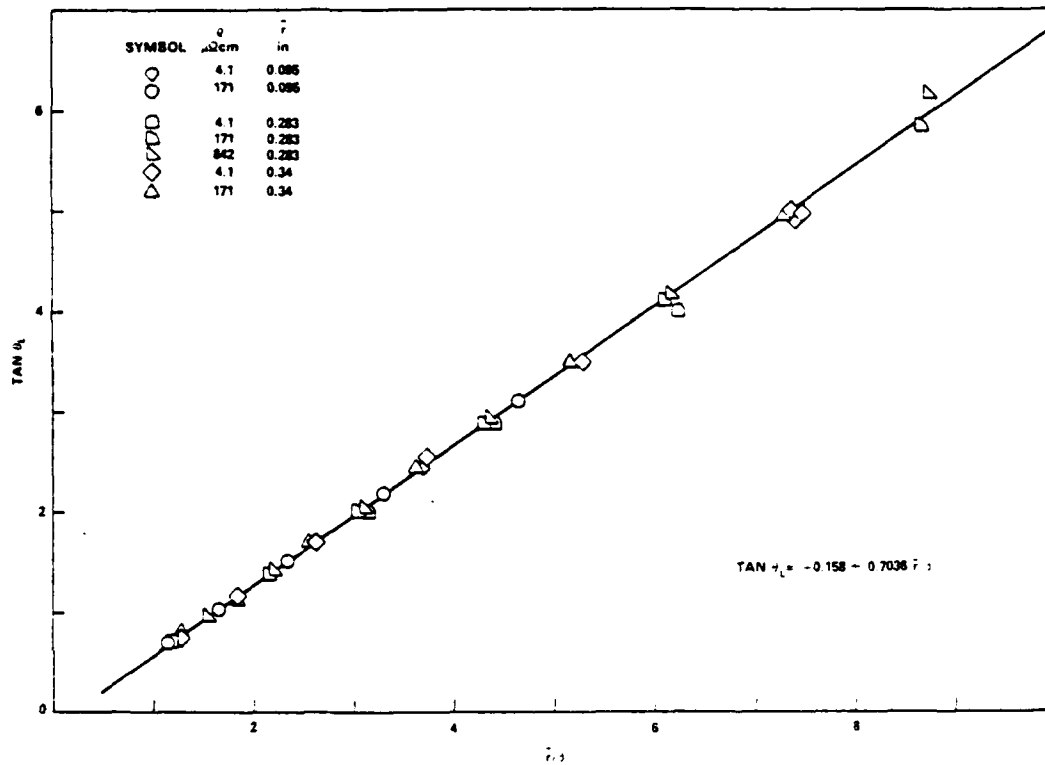
RESISTIVITY MODEL

The resistivity model is based on the independence from the coupling coefficient of the lift-off angle for ferrite cup core probes. As was noted in the previous chapter, the value of the lift-off angle depends only on the value of r/δ . Since skin depth is a function of the resistivity, it was only necessary to determine the relationship between the quantity r/δ and some convenient representation of the lift-off angle. A linear relationship was observed between the tangent of the lift-off angle and the quantity r/δ :

$$\tan \theta_L = I + m r/\delta \quad (6)$$

Data for aluminum ($4.1 \mu\Omega\text{cm}$), titanium alloy ($171 \mu\Omega\text{cm}$), and the carbon/carbon ($842 \mu\Omega\text{cm}$) are shown in Figure 13. A least squares fit to the data yielded values of I and m of -0.158 and 0.7035 , respectively.

As yet there is no theoretical support for this result. Solution of the field equations for the three-dimensional field (Figure 14a) associated with the probe is complex. However, analytic solutions have been derived for two cases where the field has been assumed, for simplification purposes, to have only one dimension in the first case and two dimensions in the second. The empirically determined constants in Equation 6 (representing a three-dimensional case) appear to be logical extensions of the constants in corresponding equations based on the analytic solutions for the one- and two-dimensional cases.

FIGURE 13. $\text{TAN } \theta_L$ VERSUS r/δ FOR FERRITE CUP CORE - 3-DIMENSIONAL CASE

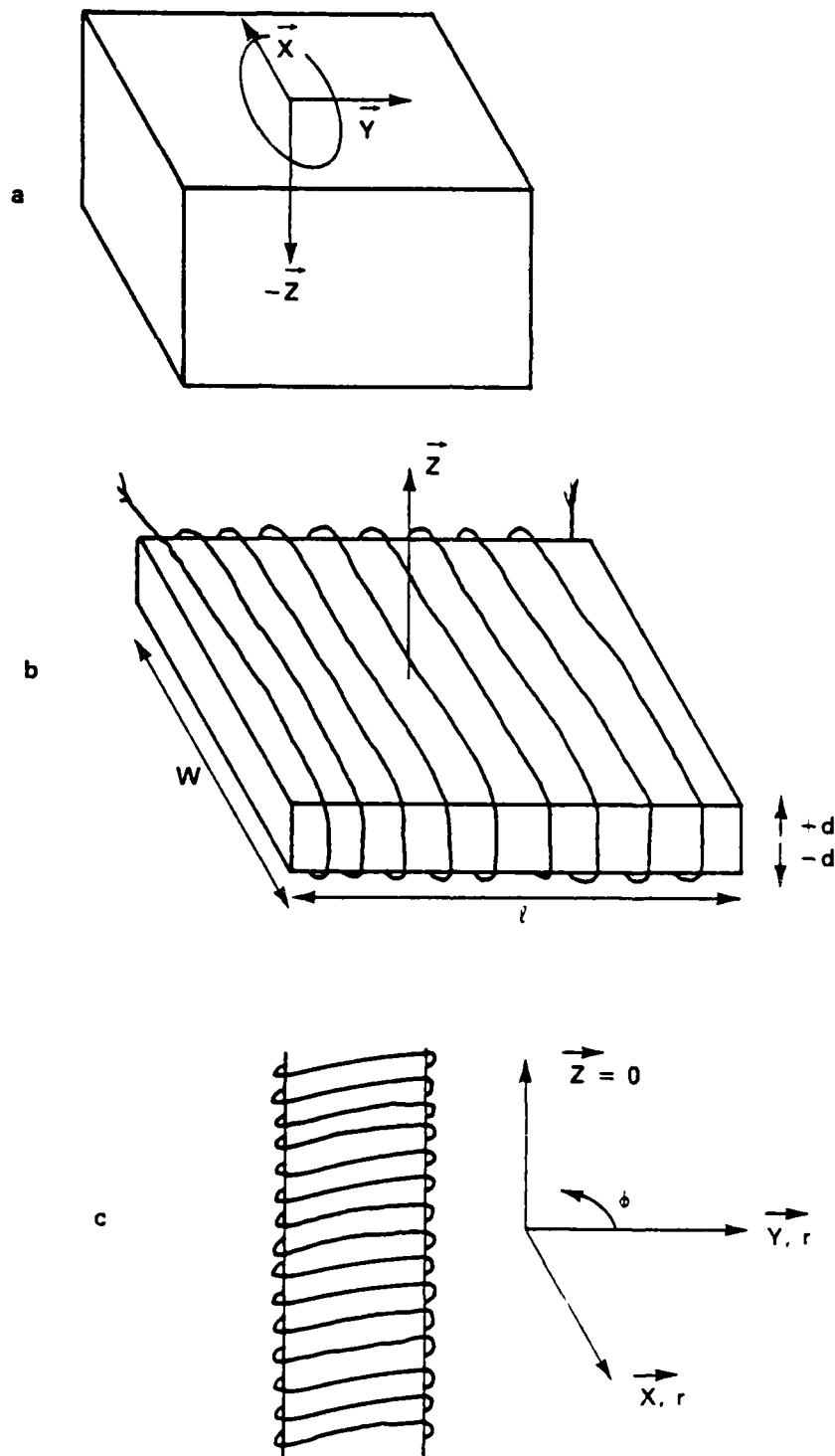


FIGURE 14. a. THREE-DIMENSIONAL FIELD (X, Y AND Z), b. ONE-DIMENSIONAL FIELD (Z), c. TWO-DIMENSIONAL FIELD (X, Y)

The one-dimensional case consists of a conducting slab subjected to a uniform magnetic field which varies only in the direction normal to the large surface of the slab (Figure 14b). The derivation of the relationship²⁹ between the probe impedance and r/δ is given in Appendix B. Using this relationship, values of $\tan \theta_L$ were calculated for a range of r/δ values and are plotted in Figure 15. A least squares fit to the straight portion of this curve (a subjective judgment) gives values of I_{1-d} and m_{1-d} of -1.650 and 2.253, respectively.

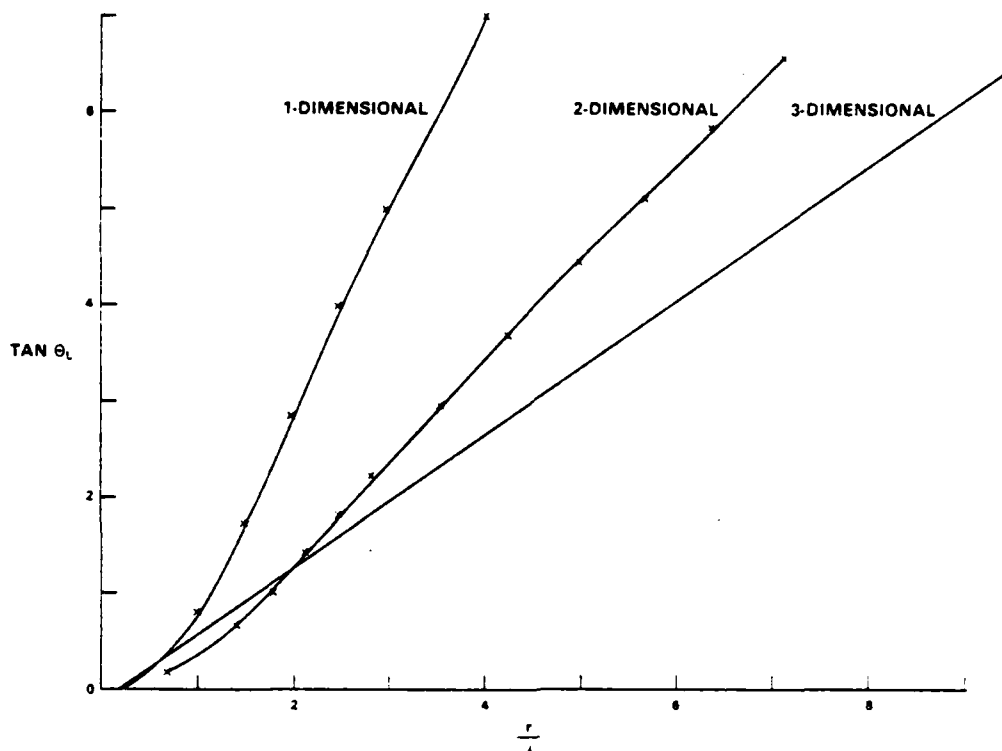


FIGURE 15. $\tan \theta_L$ VERSUS r/δ FOR 1-, 2-, AND 3-DIMENSIONAL CASES

The two-dimensional case is that of a single turn section of a uniformly energized, infinitely long solenoid encircling a conducting cylinder (Figure 14c). The relationship for probe impedance as a function of r/δ is derived in reference 14. From this relationship values of $\tan \theta_L$ were calculated for different values of r/δ and are also plotted in Figure 15. A least squares fit to the straight portion of this curve gives values of I_{2-d} and M_{2-d} of -0.904 and 1.0907, respectively.

A straight-line relationship was found to exist between the three intercept values (I) and the quantity N which describes the number of dimensions considered in each case. The correlation coefficient between the intercept values and N was 1.000. A straight-line relationship was also found to exist between the slopes (m) and the quantity $1/N$; again the correlation coefficient was 1.000. These excellent correlations may be fortuitous, but this seems unlikely given the simplicity of the relationships. It may be found that ferrite pot core eddy current probe represents an idealization of the three-dimensional case.

THICKNESS EFFECTS

When the thickness, T , of the material is less than the skin depth the eddy current response is affected. If it is known that the material thickness is greater than the skin depth, then the resistivity can be determined using Equation 6. If the resistivity is not known, it cannot always be assumed that $T > \delta$ so the potential thickness effect must be taken into account.

For purposes of discussion, the subscript P will designate "perfect" quantities, those quantities for which the thickness was greater than the skin depth and thus not a factor. The subscript E will designate quantities resulting from the thickness effect.

The thickness effect causes a smaller change in the normalized reactance ($X_E > X_P$) and a greater change in the normalized resistance ($R_E > R_P$). At any point on the impedance diagram, if the thickness were decreased the change in impedance would generate a spiral. The tightness of the spiral depends on its starting point on the impedance diagram or on r/δ . This is illustrated in Figure 16, where thickness loci,¹³ similar to those for air core probes, have been sketched. The higher the value of r/δ , the tighter the spiral.

The shape of the spiral has not been determined theoretically for the ferrite cup core probe, however some assumptions can be made on the basis of an examination of Figure 16. It appears that the angle β is related to the value of T/δ ; as T/δ decreases, β increases. The rate with which β changes with T/δ would be expected to depend on the tightness of the spiral or on its starting point on the impedance diagram quantity, indicated by r/δ .

The angle β is defined by:

$$\beta = \tan^{-1}(X_E - X_P)/(R_E - R_P)$$

Since E quantities and P quantities cannot be measured under the same conditions, the angle β is not a useful quantity. It also appears from Figure 16, that the lift-off angle θ_E is correlated with β and consequently with T/δ . Again, the relationship between θ_E and T/δ would depend on the shape of the spiral. In contrast to the angle, θ_E can be determined since

$$\theta_E = \tan^{-1}(X_E - X_P)/R_E$$

where all the quantities can be measured. A functional relationship was assumed to exist between $\tan \theta_E$ and both T/δ and r/δ . Since $\tan \theta_P$ describes r/δ , it was further assumed that the ratio of $\tan \theta$ to $\tan \theta_P$ would vary with the quantity T/δ .

Knowing the resistivity and the thickness (for purposes of model development) values of $\tan \theta_P$ were calculated from equation 4 and $\tan \theta_E$ values were measured. Values of the ratio of these two quantities are plotted against T/δ in Figure 17 for a variety of materials and r/δ values. A polynomial least squares fit to this data gives:

$$\frac{\tan \theta_E}{\tan \theta_P} = A + B\frac{T}{\delta} + C\frac{T^2}{\delta^2} \quad (7)$$

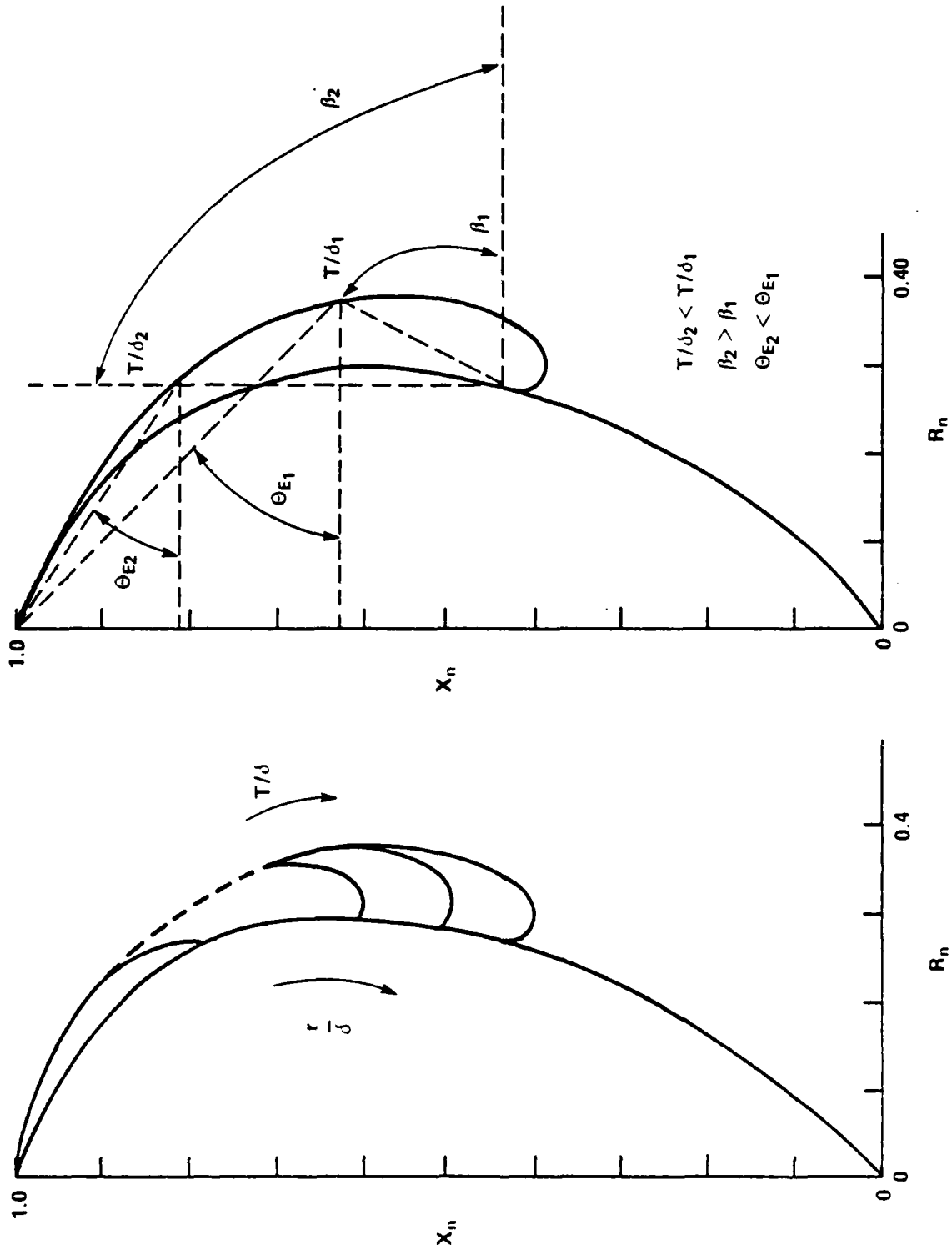
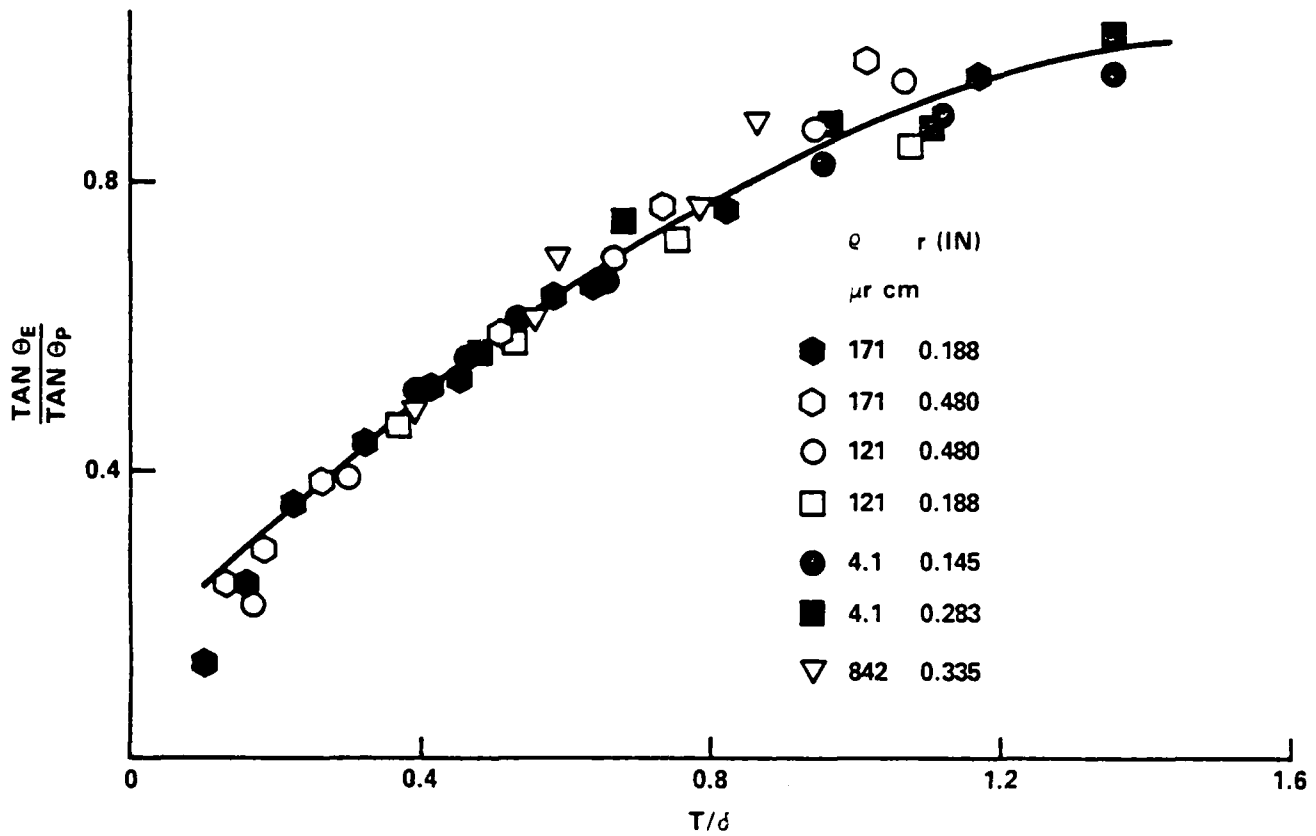


FIGURE 16. APPROXIMATION OF THICKNESS LOCI

FIGURE 17. $\tan \theta_E / \tan \theta_P$ VERSUS T/δ

where $A = 0.148$, $B = 1.0127$, and $C = -0.277$. This relationship is purely empirical but the preceding intuitive argument would indicate the existence of a theoretical foundation.

Substitution of Equation 6 and the skin depth relationship in Equation 7 and solving for ρ_E gives

$$(\rho_E)^{3/2} + C_1(\rho_E) + C_2(\rho_E)^{1/2} + C_3 = 0 \quad (8)$$

$$\text{where } C_1 = \frac{(0.0808T - 0.0526T)}{\tan \theta_E + 0.023} \epsilon^{1/2}$$

$$C_2 = \frac{-(0.1817R + 0.0112T)}{\tan \theta_E + 0.023} \epsilon T$$

$$C_3 = \frac{0.025 \tau T^2 \epsilon^{3/4}}{\tan \theta_E + 0.023}$$

Equation 8 can be solved using Newton's method of approximation with the value of ρ_p obtained from the solution of Equation 6 as the initial value.

Since the resistivity is not known, it is also not known if the skin depth is less than the thickness, and so whether it is ρ_E or ρ_p which applies. Consequently it is generally not possible to use either equation 6 or equation 8 alone. The same data are used for both equations, and it is a matter of a second or so to calculate both ρ_E and ρ_p . When these are plotted against frequency, the correct value (to within at least $\pm 10\%$) is obvious. (This selection could be implemented in software.)

Results obtained with a single probe and two materials having very different and known resistivities ($4.1 \mu\Omega\text{cm}$ and $842 \mu\Omega\text{cm}$) are shown in Figures 18 and 19. Resistivity values, ρ_p , predicted by equation 6, are presumed to be correct at those frequencies where there is no thickness effect. Resistivities, ρ_E , predicted by equation 8, are presumed to be correct at lower frequencies where the skin depth is greater than the thickness. The two curves cross at approximately that frequency where $T = 1.4\delta$. This would be expected from an examination of Figure 16, where the ratio of the tangents approached unity at $T/\delta = 1.4$.

APPLICATION TO GRAPHITE EPOXY

Three types of graphite epoxy were investigated to determine the effects of material fiber type and weave on eddy current-material interaction. The material was purchased in pre-preg tape or cloth form and panels fabricated with $\{0,90,0\}_s$ ply order. The panels varied in thickness from 0.039 inch (0.96 mm) to 0.139 inch (3.53 mm). The materials were a 5-harness satin weave (pan fibers) supplied by Hercules, Inc. (A370-5H/3501-6), a pan fiber (CE 9000-9/Celion 6000) and a pitch-based fiber (CE 9000-9/P55S), both supplied by Ferro Composites, Inc. Dr. C.V. Dodd²³ measured the resistivity of one of the satin weave panels at 100 kHz ($9156 \mu\Omega\text{cm} \pm 2\%$) and at 2 MHz ($14426 \mu\Omega\text{cm} \pm 2\%$).

When the model was applied to the specimen whose resistivity had been determined by Dr. Dodd, the estimated resistivity values were 55 percent too low. It was found that if the values of the geometric quantities (probe radius and material thickness) were multiplied by $\sqrt{2}$, the model accurately estimated the resistivities of all the graphite epoxy materials. "Accuracy" was assumed if use of the estimated resistivity values provided agreement with the depth model in the following chapter. If the correction factors are used when the resistivity model is applied to a graphite epoxy material, then the depth model can be used, without modification, to measure depth of damage in graphite epoxy.

As mentioned earlier, the need for these correction factors for graphite epoxy may mean that additional factors are involved in application of the model to high resistivity materials. Or it may be related to the more complex conduction mechanisms in these particular composite materials. If this is true, then further investigation of these effects might shed some light on the conduction mechanisms in graphite epoxy.

Resistivity values (ρ_E and ρ_p) estimated for a panel of the pan fiber satin weave material are plotted against frequency in Figure 20. Also included in the figure is a straight line connecting the two resistivity values determined by Dodd

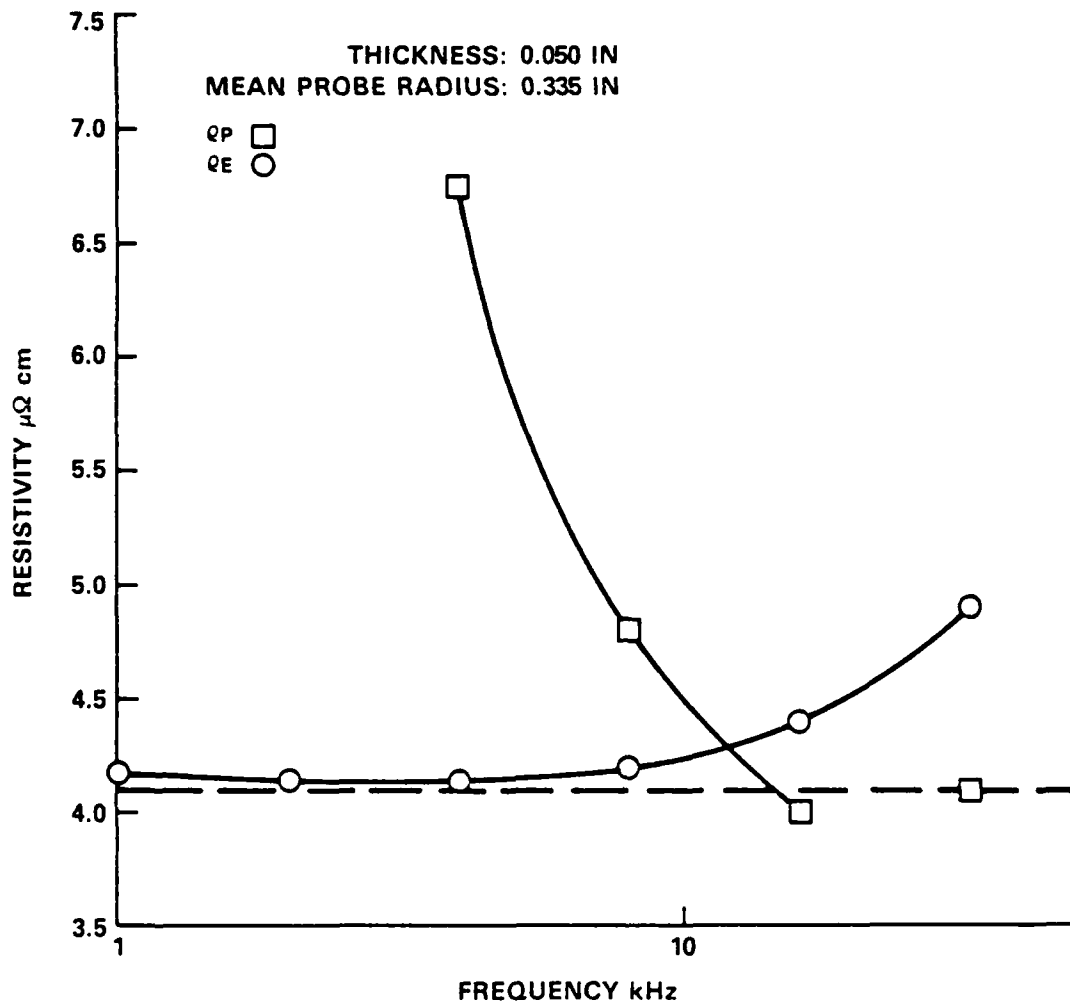


FIGURE 18. Q_P AND Q_E VERSUS FREQUENCY FOR ALUMINUM

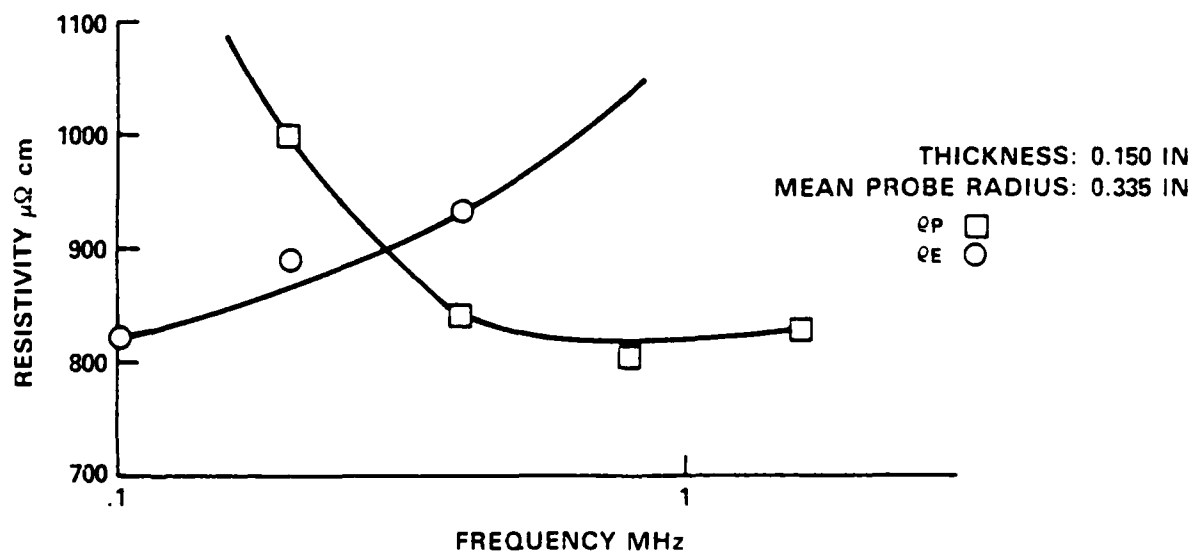


FIGURE 19. Q_P AND Q_E VERSUS FREQUENCY FOR CARBON/CARBON

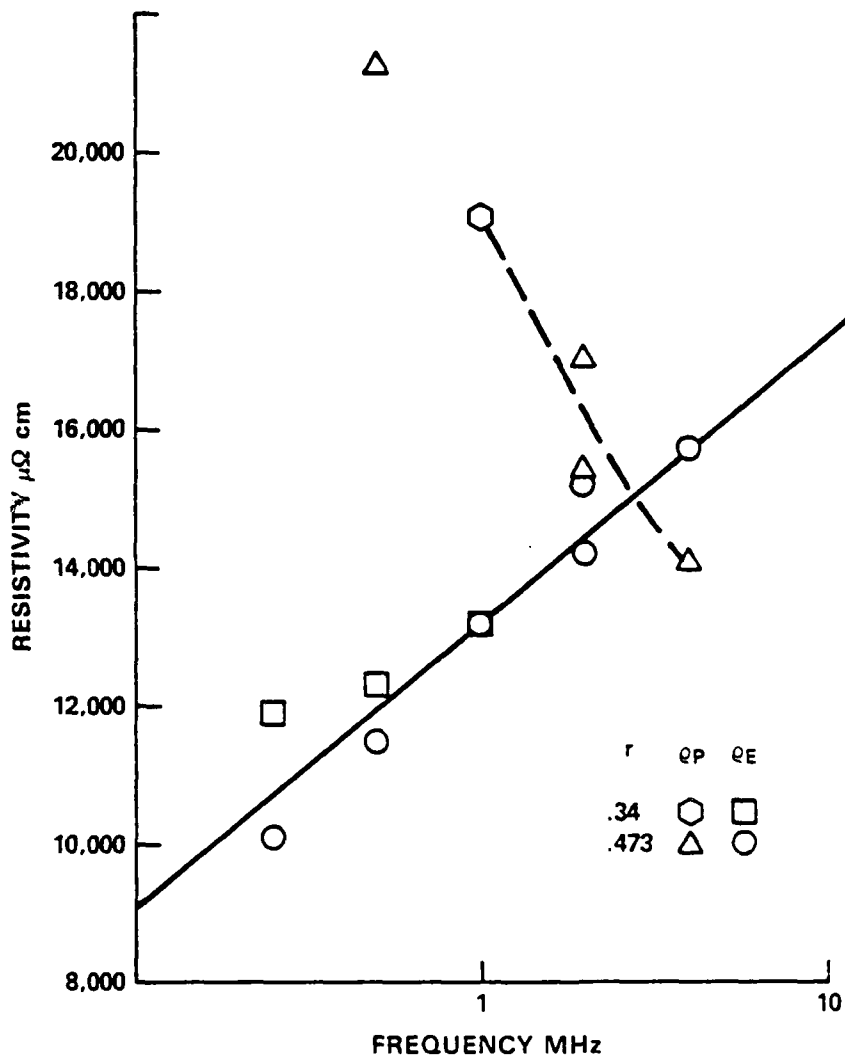


FIGURE 20. Q_P AND Q_E VERSUS FREQUENCY FOR PAN FIBER SATIN WEAVE GRAPHITE EPOXY

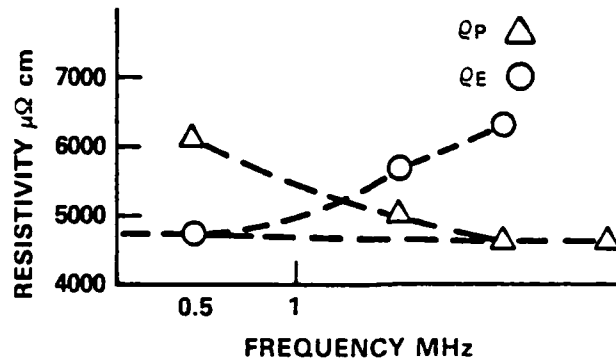


FIGURE 21. ρ_P AND ρ_E VERSUS FREQUENCY FOR PITCH BASED GRAPHITE EPOXY

and extrapolated to 10 MHz. The experimental values fall within $\pm 10\%$ of this line, except above 2 MHz. The greater difference above this frequency may be experimental error, or it may be that the resistivity levels off above 2 MHz.

The two resistivity estimates for a specimen of the pitch-based fiber tape material are plotted against frequency in Figure 21. On the basis of these curves, the resistivity was estimated to be constant at $4600 \mu\Omega\text{cm}$ from 0.5 through 8 MHz.

The estimated resistivities values for a specimen of the pan fiber tape material are shown in Figure 22. Here the resistivity appears to be constant at about $8900 \mu\Omega\text{cm}$ up to 1 MHz where it begins to increase with frequency. This type of behavior is not unusual in graphite epoxy.¹²

EDDY CURRENT CONDUCTION IN GRAPHITE EPOXY

Measurement of broken-fiber damage in graphite epoxy requires knowledge of the resistivity of the good material surrounding the damaged region, but there is no requirement to understand the mechanisms that cause resistivity to assume this particular value. The possible sample-to-sample variation in resistivity and the possible dependence of this property on frequency indicate there are subtle characteristics of the material which have strong effects on resistivity. These same characteristics may also affect other properties of the material. If the relationships between the measured resistivity and the properties of the material were understood and if the conduction mechanisms were understood, then it could be possible to measure other properties of a particular sample via measurement of the resistivity and its frequency dependence. A conduction mechanism model could be a useful tool in evaluating a particular sample; however, development of the model will not be a simple task.

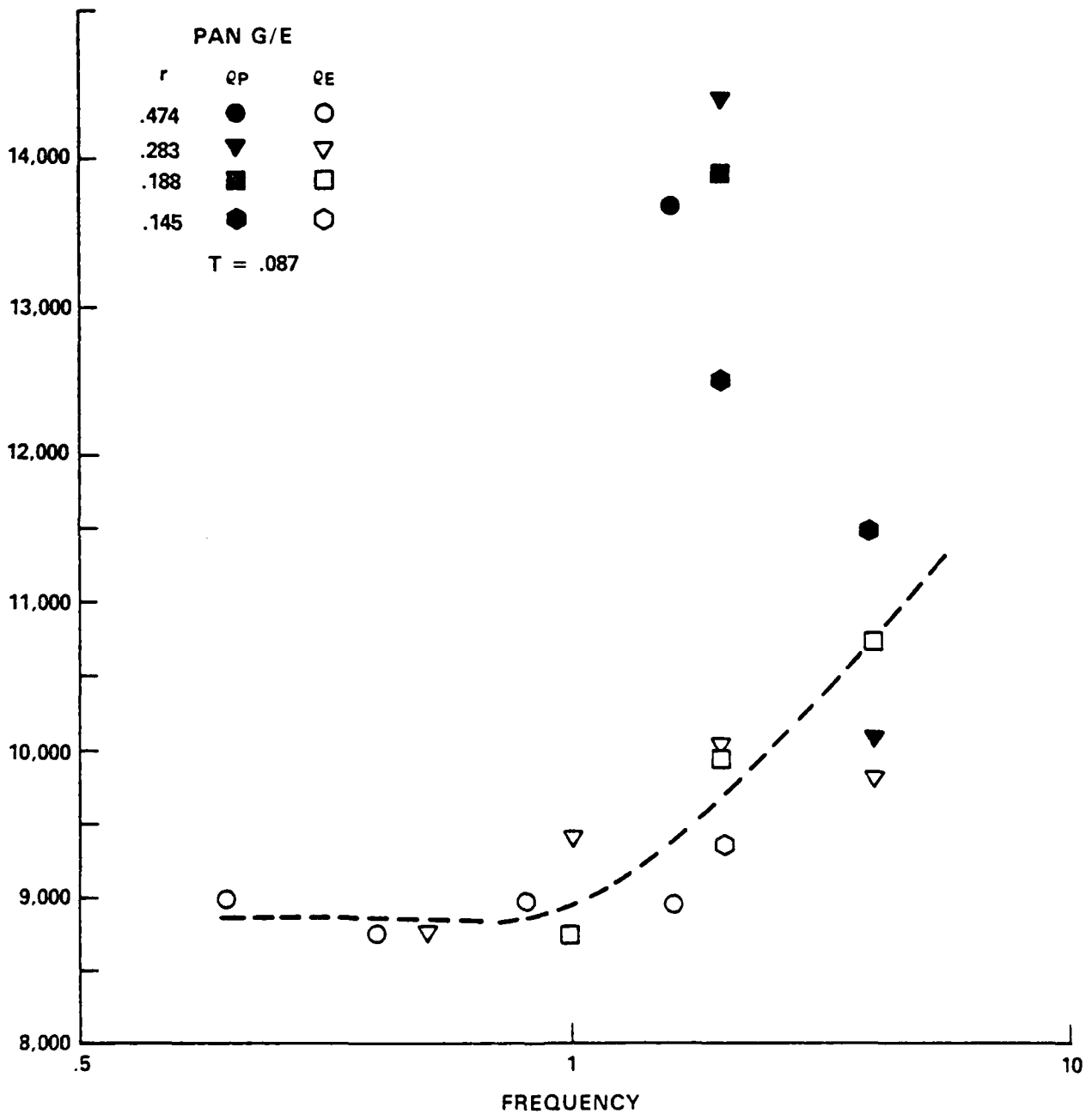


FIGURE 22. ρ_p AND ρ_E VERSUS FREQUENCY FOR PAN FIBER GRAPHITE EPOXY

Such a model for graphite epoxy will have to accommodate some apparently conflicting observations. The conductivity of some samples, as measured by two eddy current methods and by a two-point contact method, decreases with increasing frequency. Neither the conductivity of the fibers alone, nor the low (3.4) relative permeability of the nonconducting pure epoxy showed a frequency dependence.¹² Both the conductivity values and the frequency dependence of the conductivity varied among different samples. Inter-fiber capacitive coupling would be expected to vary with fiber density and would explain the sample to sample variation. However, inter-fiber capacitive coupling would result in an increase in conductivity with frequency, rather than the reverse which was observed. In view of the apparent difficulty in resolving these observations, it is fortunate that the application of eddy current to the detection and measurement of broken-fiber damage does not require an understanding of the conduction mechanism.

CHAPTER 5

DETECTION AND MEASUREMENT

INTRODUCTION

There are two goals in the NDI of a material: detection of the damage and measurement of its size. A defect is detected if its signal can be discerned from the background noise. (In this case noise refers to the extraneous variations of the signal, and not necessarily to thermal noise energy.) This imposes certain requirements on the size of the probe and the inspection frequency (frequencies).

The term "measurement" is somewhat more complex. As was mentioned in the introduction, damage sustained by graphite epoxy consists of varying densities of delamination and broken fibers. The damage may break both surfaces, either surface, or neither. Since the volume of the damage determines the extent to which the material has been weakened, ideally we would like to measure the amount of good or undamaged material between the damage and each of the surfaces as well as the planar extent of the damage (area of damage in planes parallel to the surface). The ability to measure the thickness of the good material between the inspected surface and the damage depends on proper selection of probe size and frequency. Accurate measurement of the planar extent or area requires that the resolving power of the probe be maximized, given the constraints imposed by the requirements both to detect and damage and to measure its depth.

PROBE SIZE AND FREQUENCY

The relationships among probe size, frequency, and material resistivity determine our ability to detect and measure damage. To detect damage near the back surface of the material, the skin depth should be slightly greater than the thickness of the material. So the operating frequency (or the mid-frequency when several frequencies are used for measurement) is established by the resistivity of the material and its thickness. If it were possible to use this frequency and a tiny probe, we could measure damage throughout the thickness and with good planar resolution. However, as the ratio of r/δ decreases below unity, the impedance rapidly approaches the top of the impedance curve where defect responses become increasingly small (Figure 7). The optimum value of probe size depends on the detection method and the trade-off between resolution and defect sensitivity that is desired.

DETECTION AND AREA MEASUREMENT

Both detection and measurement of the planar extent of damage can be implemented by raster scanning the probe across the surface of the test material and measuring the changes in probe impedance.

A schematic of a typical eddy current scanning system is shown in Figure 23. The eddy current instrument energizes the coil with an RF signal. Since small impedance changes are of interest, typical eddy current instruments subtract the impedance of the probe when it is in contact with good material. Often this is achieved by a bridge circuit, where one arm of the bridge is a coil similar to the test coil. This differential measurement is represented by a spot in the center of the impedance plane displayed on the CRT. An X-Y scanning device raster scans the probe over the surface of the material, and changes in the impedance are displayed on the CRT. Orthogonal components of the impedance (usually not identified as resistive and reactive components) are available as analog output voltages either to provide a signal to the C-scan pen or for digitization and further analysis. This system can be implemented by the modification of a commercial ultrasonic C-Scan system to incorporate a spring-loaded eddy current probe in conjunction with a commercial eddy current instrument.

Because of inaccurate phase detector response at higher frequencies, the typical eddy current instrument does not provide values of sufficient accuracy to permit meaningful analysis. For this reason, a commercial impedance analyzer was used in this project to collect data for analysis. The accuracy of commercial eddy current instruments was found to be sufficient for C-scan generation.

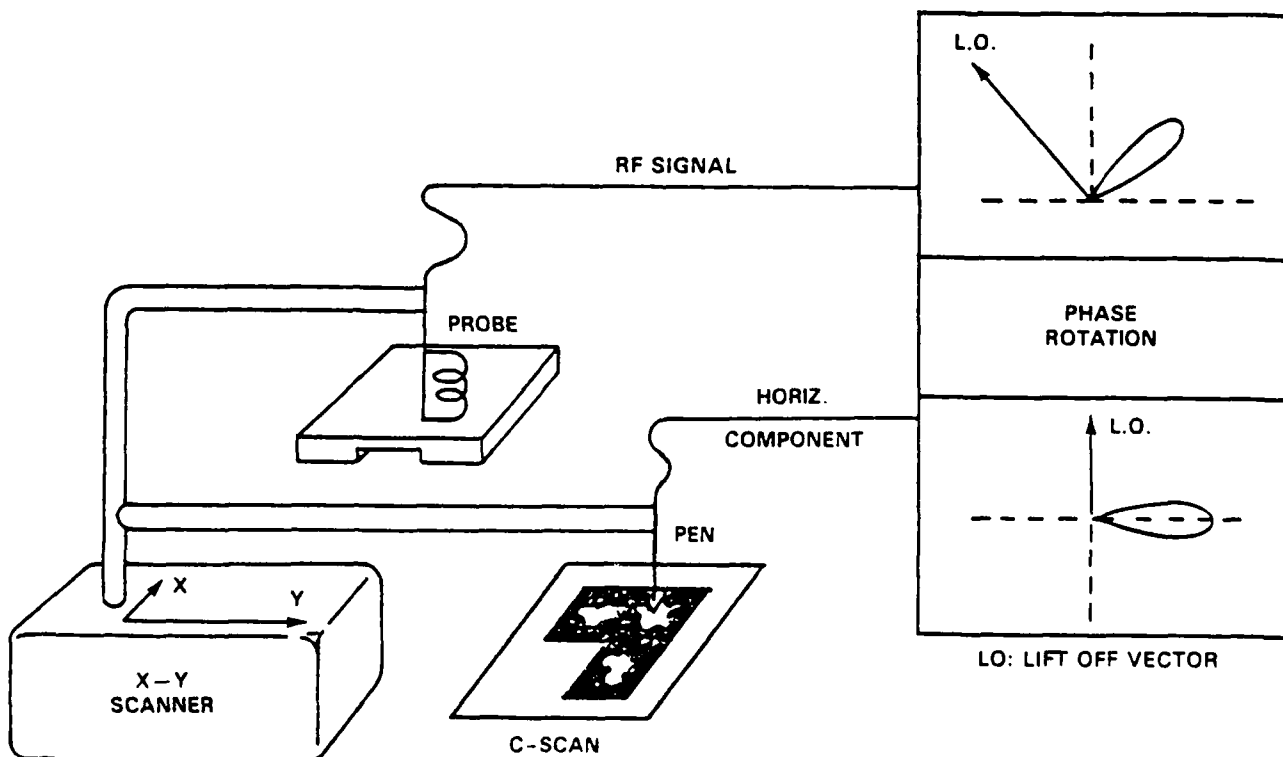


FIGURE 23. SCHEMATIC OF EDDY CURRENT C-SCAN SYSTEM

As the probe is scanned across the surface, irregularities in the surface can cause variations in the separation between the probe and material; these variations in turn cause deflections in the direction of the lift-off vector. To avoid mistaking these lift-off deflections for defect indications, the eddy current instrument provides for the arbitrary rotation of the phase of the impedance plane so the lift-off vector can be aligned along one of the orthogonal axes. The component of the response that is orthogonal to the lift-off vector, or the O-component, provides the signal to the pen. The changing voltage in the pen, associated with the changing magnitude of the O-component of the impedance, provides a map of the damage in the material. Since an increase in impedance (or a decrease depending on relative orientation of the lift-off vector) is associated with a damaged region, an image of the planar extent of the damaged region is shown on the map or C-scan.

The sensitivity of the system depends on the magnitude of the O-component of the defect response and this is determined by location on the impedance diagram, or on the ratio r/δ . The effect of r/δ on the relative magnitudes of the O-components is illustrated in Figure 24 where defect response vectors are shown as well as their projections on the O-axis. The numbers labeling the responses indicate depth, with #3 as the deepest. It can be seen that for those defects considered, the magnitudes of the O-components are strong for r/δ values between 1.6 and 3.3 (locations B through D). Furthermore, at these r/δ values (in contrast to $r/\delta = 1.2$) the

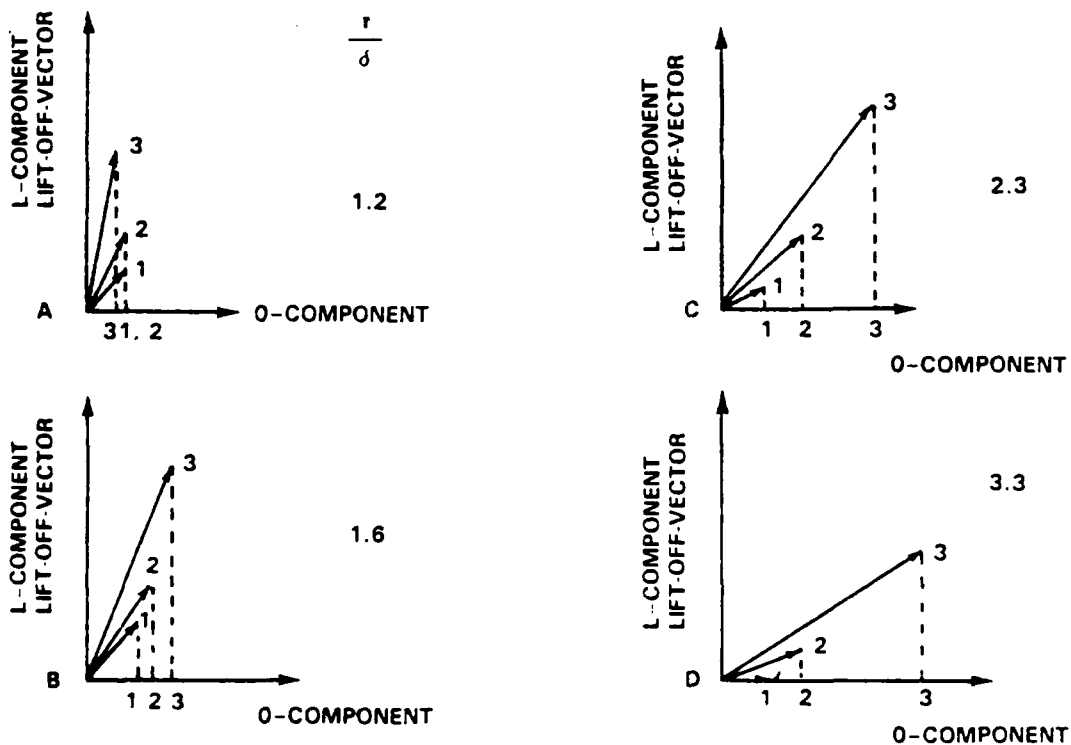


FIGURE 24. RELATIONSHIPS BETWEEN O-COMPONENT OF DEFECT RESPONSE AND r/δ

magnitudes of the O-components are proportional to the depth of the defect. This, of course, will translate to a variation in grey tone (or color in a computerized system) with depth of damage.

For maximum planar resolution (smallest possible probe) without a sacrifice in magnitude of the O-component ($r/\delta > 1.5$) an r/δ value of about 1.5 would be optimum. Since skin depth should be on the order of material thickness, the probe radius should be about half again the thickness of the material. So, while the high resistivity of graphite epoxy permits the inspection of greater thicknesses than are usually associated with eddy current inspection, there is a trade-off in lower planar resolution. The strength of thick materials will probably not be as sensitive to small defects but this will have to be determined by the design engineers.

Some examples of both eddy current and ultrasonic C-scans are shown in Figures 25 through 27. In Figure 25 the indications of the impact-damaged regions appear to be very similar; however, the area of the eddy current indication was enlarged by the 0.86-inch (22 mm) diameter of the probe. The actual size of the region containing the broken fibers can thus be assumed to be much smaller than the area of the indication in the eddy current C-scans and, consequently, much smaller than the delaminated region shown in the ultrasonic C-scan.

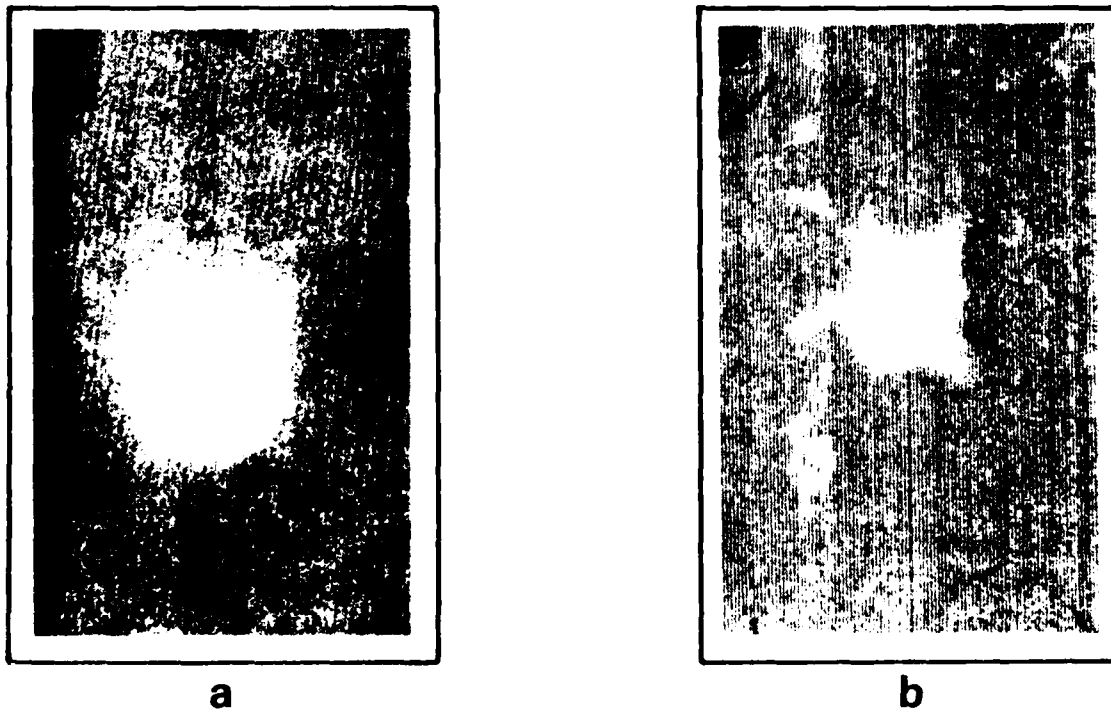


FIGURE 25. EDDY CURRENT (a) AND ULTRASONIC (b) C-SCANS OF AN IMPACT DAMAGED GRAPHITE EPOXY PANEL



FIGURE 26. ULTRASONIC (UPPER) AND EDDY CURRENT (LOWER) C-SCANS SHOWING DAMAGE IN A FILAMENT WOUND CYLINDER HAVING A 0.6 m (15.2 mm) THICK WALL

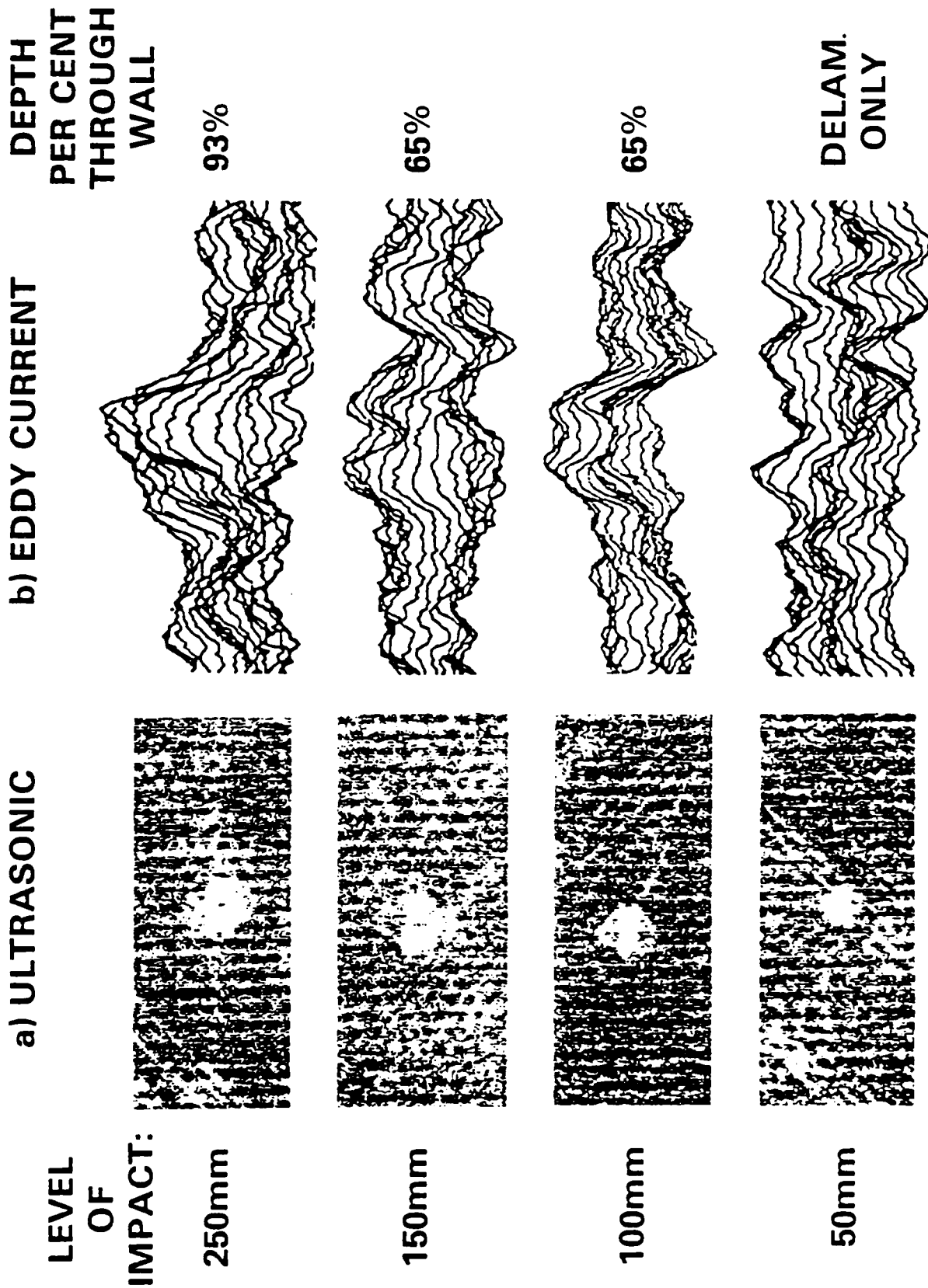


FIGURE 27. EDDY CURRENT AND ULTRASONIC C-SCANS OF IMPACT DAMAGED PANEL WITH HONEYCOMB BACKING

The C-scans shown in Figure 26 are those of a filament-wound cylinder which had been damaged by pressure loading. The cylinder was 8 inches (20.3 cm) high and its outside diameter was also 8 inches. The wall thickness was 0.6 inch (15.25 mm). The cylinder was mounted on the turntable of a Testech computer controllable scanner. The eddy current probe and the ultrasonic transducers were mounted on the scanner which axially scanned the cylinder. (The tank was empty for the eddy current C-scan and filled with water for the ultrasonic C-scan.) Details of the instrumentation and procedure are provided in reference 30.

The C-scans represent unwrapped views of the cylinder wall. In the through-transmission ultrasonic C-scan, the many light areas indicate delamination. In the eddy current C-scan, the blue areas indicate a strong response in the O-direction. Since it has not been possible to detect thin delaminations with eddy current (delaminations being in the plane of current flow), it was assumed that the blue areas on the C-scan represent regions of broken fiber damage. The areas of the indications of broken-fiber damage in the eddy current C-scan are larger than the actual area of the region containing the broken fiber damage by an amount proportional to the 1.5-inch (43.1 mm) diameter of the eddy current probe.

The blue region in the lower center portion of the eddy current C-scan corresponds to the white indication of a delamination in the ultrasonic C-scan. Similarly, the larger V-shaped blue region on the left end of the eddy current C-scan may be associated with the similarly shaped "white" region in the ultrasonic C-scan. While it is not possible to evaluate the relative severity of the various delaminated areas from the ultrasonic C-scan alone, in combination with the eddy current C-scan, it appears possible to identify which of the delaminations were sufficiently severe to result in broken fibers.

In Figure 27, the ultrasonic (through-transmission) and the "hidden line" eddy current C-scans of the impact damaged honeycomb-backed panel indicate the presence of both delamination and broken-fiber damage for impact levels of 250 mm, 150 mm, and 100 mm. At the 50-mm impact level, the absence of an eddy current indication, when the ultrasonic C-scan showed delamination, signifies that the delamination was insufficiently severe to result in fiber breakage. The "waves" surrounding the damage indications in the eddy current scans were attributed to surface irregularities. This panel was provided by courtesy of the Australian Aeronautical Research Laboratory.

DEPTH MEASUREMENT

Measurement of defect depth depends on the skin effect. According to the skin depth relationship, the phase of eddy currents at a distance from the surface lags those at the surface by an amount equal to the ratio of that distance to the skin depth¹³ or

$$\theta \text{ (rad)} = a/\delta$$

In a similar manner, the phase angle of the response to a defect located at a distance, a , (defined in Figure 1) from the surface depends on the ratio a/δ . The magnitude of the defect response also depends on a/δ . The effects of defect depth on both the phase angle and the magnitude of the defect response are illustrated in Figure 28.

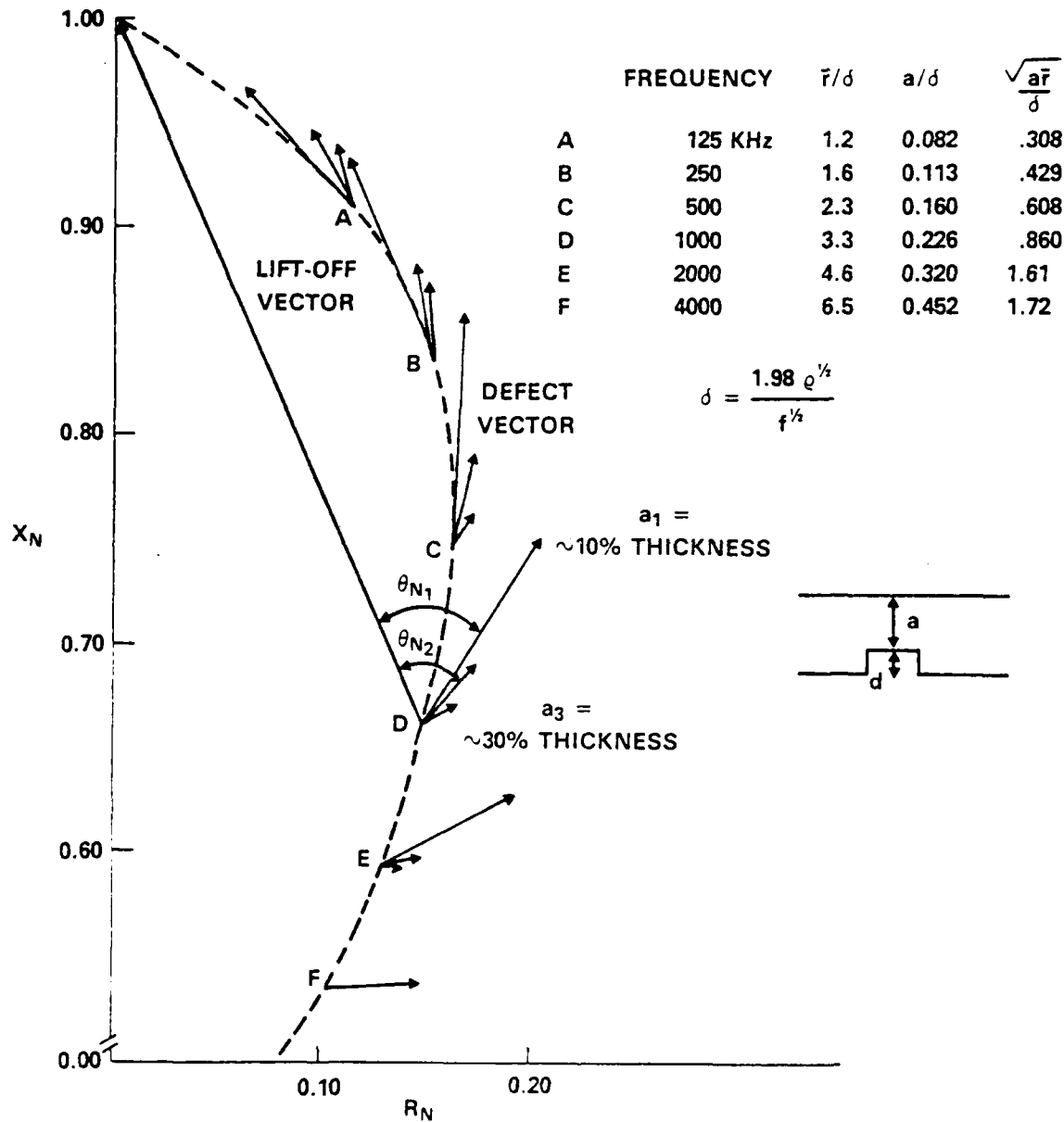


FIGURE 28. EFFECT OF DEFECT DEPTH ON DEFECT RESPONSE.

Typically³¹ in the measurement of defect depth in metals, a calibration standard containing artificial "cracks" of known depth is used to generate a curve relating the phase angle or magnitude of the defect response with depth (d) of the artificial crack. A separate curve usually is required for each probe and frequency.

At any given value of r/δ , the magnitude of the response to a particular defect depends not only on the depth of the defect but also on the coupling coefficient of the probe that is used. In contrast, because the lift-off angle is independent of the coupling coefficient for ferrite cup core probes (in the absence of shielding effects), the phase angle of the defect response, at any given value of r/δ , depends only on the depth of the defect and is independent of the particular probe that is used. For this reason, the phase angle relationships were used in the depth model.

To provide a basis for comparing the phase angles of defects at different depths the defect phase angle, θ_D , can be normalized with respect to the lift-off angle θ_L , or

$$\theta_N = \theta_D - \theta_L$$

where θ_N is the normalized defect phase angle. The lift-off angle is given by

$$\theta_L = \tan^{-1}((1 - X_n)/R_n)$$

where X_n and R_n are the normalized imaginary and real components of the lift-off response. The defect phase angle is given by

$$\theta_D = \tan^{-1}(X_D - X_m)/(R_m - R_D)$$

where X_D and R_D are the imaginary and real components of the defect response at that point where its magnitude is greatest as the probe is scanned over the defect; X_m and R_n are the corresponding components of the defect-free material.

In Figure 28, it can be seen that as the base point (normalized impedance on good material) moves down the impedance curve, as r/δ increases, the normalized phase angle, θ_N increases. Although it is not obvious in the figure, at any point on the impedance curve (for any value of r/δ) the angular separation between defect responses depends on a/δ . The quantity r/δ appears to determine the extent to which the quantity a/δ affects the phase angle of the defect response. A strong correlation was observed between θ_N and the square root of the product of the quantities r/δ and a/δ (Figures 29 through 31).

Data for both flat bottom holes (FBH) and saw cuts or notches in aluminum and for FBH in both the titanium alloy and the carbon/carbon are plotted in Figure 29. A polynomial least squares fit to these data gave

$$\theta_N = A + B \sqrt{\frac{ar}{\delta}} + C \frac{ar}{\delta^2} \quad (8)$$

where $A = -24.73$, $B = 113.21$, and $C = -17.49$. When this is solved for a , the two resulting values differ by several orders of magnitude so there is no question as to which is the appropriate value. This relationship applied to values of the quantity \sqrt{ar}/δ between 0.2 and 2.0 (or for values of ar/δ^2 between 0.04 and 4.0). There is no reason to assume this is the theoretical limitation to the range of applicability

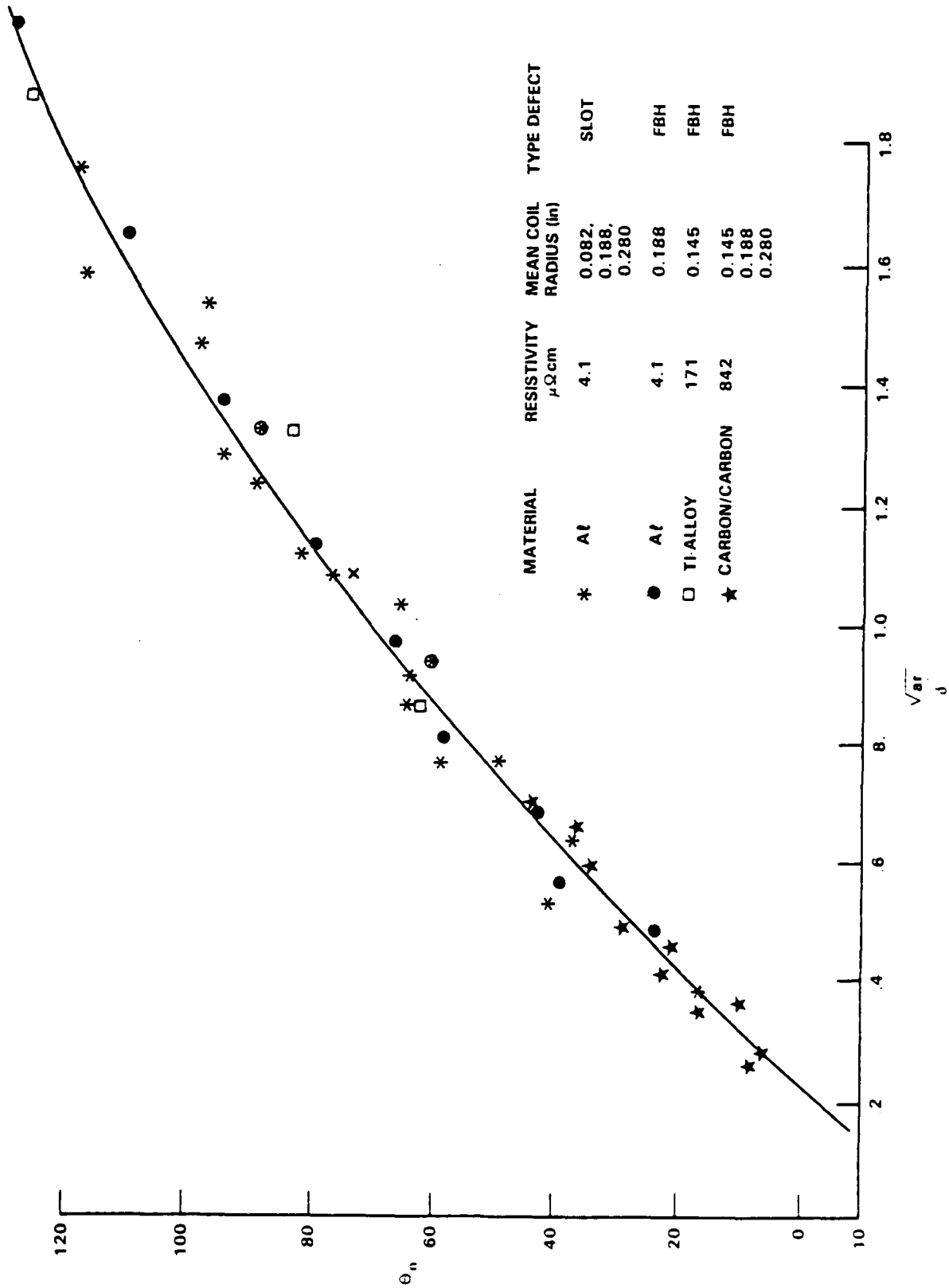


FIGURE 29. NORMALIZED DEFECT PHASE ANGLE VERSUS $\sqrt{ar/d}$ FOR METALS AND A CARBON/CARBON

of the model. The upper limit of 4 for the quantity ar/δ^2 results from limitations in instrument resolution. When either of the two components of the impedance were small, error in their measurement resulted in larger errors in the calculated phase angles. When r/δ is greater than about 6 (Figure 3) the change in the resistive component is much smaller than the change in the reactive component. Since the magnitude of the larger quantity determined the resolution, errors in the resistive component and in the angle resulted. A value of 0.75 for the quantity a/δ was found to be the practical limit for the instrumentation used. The product of 0.75, the practical limit for a/δ , and 6, the practical limit of r/δ , is 4, the maximum value for which meaningful data were obtained.

Similar data for FBH in the satin weave material are shown in Figure 30 along with the curve described by Equation 1. These data were collected with a single probe ($r = 4.78$ mm). The thicknesses of the panels containing the defects varied by a factor of almost 4 and the FBH varied in diameter from 3 mm to 25.4 mm. The average scatter in these data was $\pm 3.8^\circ$, as it was for the metal and carbon/carbon data shown in Figure 29. Data for FBH in the pitch-based material are shown in Figure 31 along with data from both FBH and notches in the pan material. These data were taken with two probes having mean radii of 3.7 and 4.8 mm. The average scatter in these data was $\pm 3.8^\circ$. However, taken alone, the average error in the notch data was $\pm 5^\circ$. This apparent error may not be significant but it is systematic and may represent a geometry effect. It is not clear why there should be a geometry effect for defects in graphite epoxy, but not for those in metals.

Two observations can be made regarding these results. First, while a thickness-to-skin depth ratio less than unity has a strong effect on the lift-off angle θ_L , it appears to have no effect on the difference between the lift-off angle, θ_L , and the defect angle, θ_D . In order to obtain strong responses from all the defects, well over half the data were taken at frequencies such that the skin depth was greater than the thickness of the material containing the defects, yet no effect was observed.

Second, the results appeared to be independent of the relative sizes of defect and probe. The diameters of the FBH varied from 0.125 inch (3.18 mm) to 1.0 inch (25.4 mm) and ratios of FBH diameter to probe diameter ranged from 0.5 to 6. In all cases the slots were longer than the probe diameter and their width was between 0.014 inch (0.36 mm) and 0.030 inch (0.76 mm). It was concluded that for the defect geometries considered, all of which broke the back wall, defect geometry was not a significant factor in the phase angle of the defect response. It is possible that geometry effects were overshadowed by experimental error.

ERROR ANALYSIS

The percent error in a can be determined by differentiation of equation 8 giving

$$100 \frac{da}{a} = d\theta / \frac{B/\sqrt{ar}}{\delta} + C \frac{ar}{\delta^2} \quad (2)$$

An error in measurement of the resistivity is reflected as an equivalent error in a . The scatter in θ_N , and consequently the uncertainty in θ_N , is about $\pm 4^\circ$, regardless of θ_N , so the resultant error in a depends on \sqrt{ar}/δ as shown in

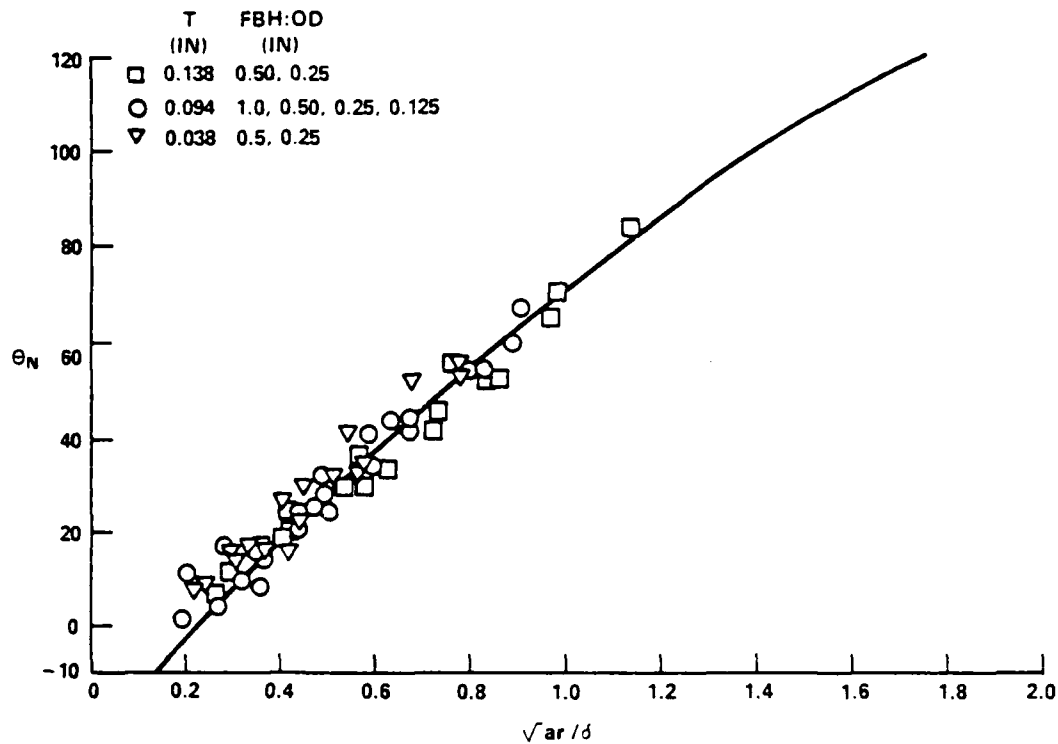


FIGURE 30. NORMALIZED DEFECT PHASE ANGLE VS \sqrt{ar}/δ FOR SATIN WEAVE GRAPHITE EPOXY

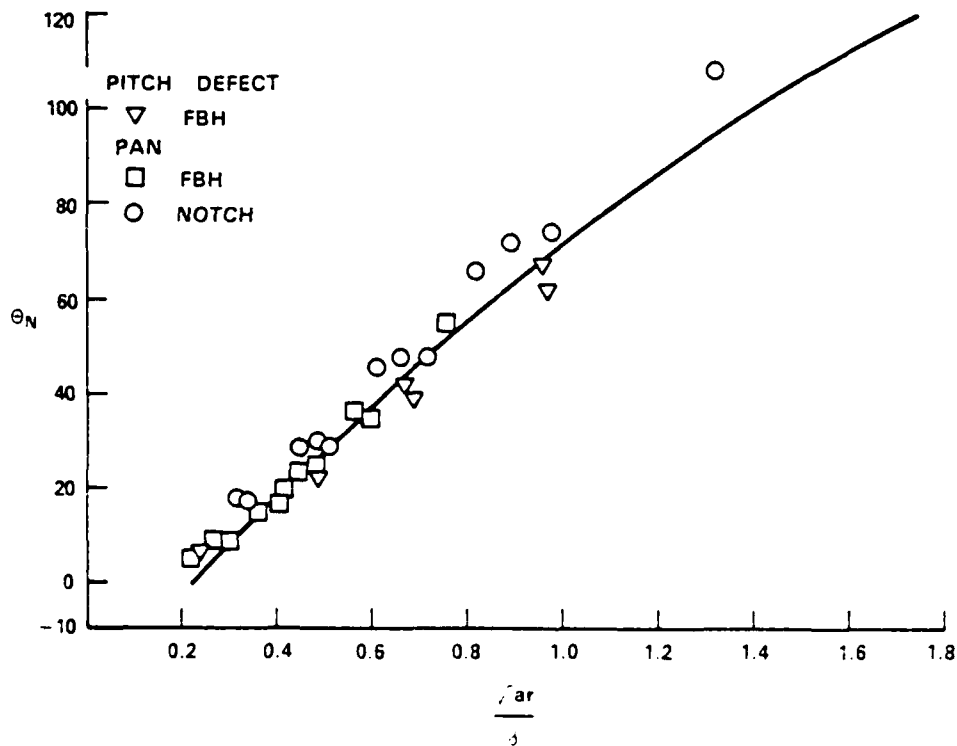


FIGURE 31. NORMALIZED DEFECT PHASE ANGLE VERSUS \sqrt{ar}/δ FOR PITCH FIBER TAPE MATERIAL AND PAN FIBER TAPE MATERIAL

equation 9. The percent uncertainty in \underline{a} for a 4° uncertainty in θ_N is plotted against \sqrt{ar}/δ in Figure 32. There is a broad minimum in the error for values of \sqrt{ar}/δ between about 1.0 and 2.2. This provides a strong argument for a multifrequency approach. Measurement of \underline{a} at the highest frequency for which there was a repeatable response would result in a maximum uncertainty of about $\pm 10\%$, assuming an uncertainty in θ_N of $\pm 4^\circ$.

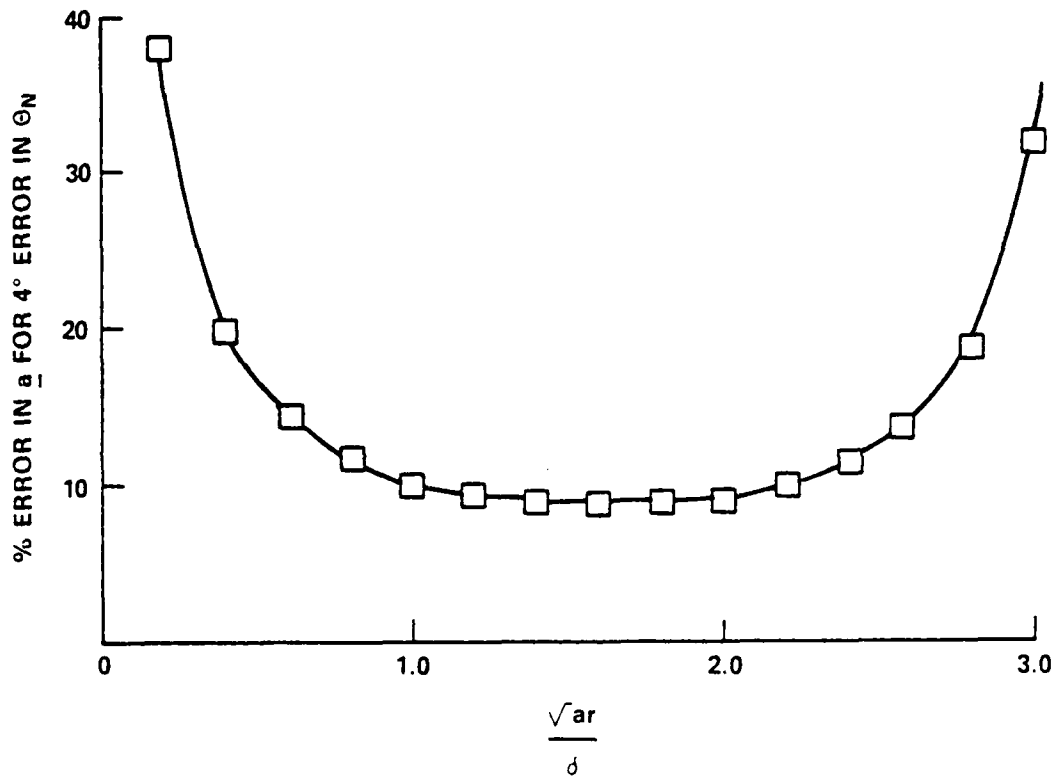


FIGURE 32. PERCENT ERROR IN \underline{a} VERSUS \sqrt{ar}/δ

CHAPTER 6

DISCUSSION AND SUMMARY

AREAS REQUIRING FURTHER ATTENTION

The depth model was based on data from artificial defects: saw cuts and flat bottom holes, all of which broke the back surface. Before the model can be applied with any confidence to impact damage, it must be tested on samples containing impact damage. The samples must then be destructively analyzed to determine the exact through-thickness of the broken fiber damage. Ultrasonic A-Scans can provide information on the through-thickness location of delamination, but it is probable that broken fibers would be located further from the impact surface (deeper) than the nearest delamination. Sectioning the specimen at the damage location might be sufficient if the section were made at the precise location of the broken fibers. A more exact method for locating damage in graphite epoxy has been developed by Freeman.³² This deplying technique involves heating the specimen to a temperature such as to partially pyrolyze the matrix. The individual plies can then be separated to expose the fibers adjacent to the interface. Sufficient matrix remains to hold the broken fibers in place so the exact through-thickness location as well as the planar distribution of the broken fibers can be determined.³³

Before eddy current methods can be conveniently used to inspect for impact damage in graphite epoxy components at the depot level, several problems will have to be addressed. A portable X-Y scanning device or a spatial locator interfaced with an appropriate eddy current instrument is required. An eddy current instrument with phase detector outputs that are accurate at frequencies above 500 kHz would improve defect detectability and is a requirement for depth measurement. Both of these problems are among those being addressed in several Small Business Innovative Research projects.

Development of a through-transmission eddy current system to inspect thick-wall (greater than 1.0 inch or 2.54 cm) cylinders could provide greater sensitivity to damage in situations where both surfaces were accessible. Such a system could be used to inspect for service-incurred damage in cylinders and would provide for in situ monitoring of the onset and growth of damage during materials development stage testing. This system is under development at the Naval Surface Warfare Center.

More information about the damage could be obtained by analysis of all of the information available in the eddy current response. Time in this project did not permit analysis to the extent required of both the phase angle relationships and the magnitude relationships. Only the phase angles were analyzed in-depth as they appear to emphasize the most important information. The normalized phase angle of the defect response measured where the magnitude is greatest appeared to depend only on the distance of the damage from the surface (depth) and not on the planar extent of the damage regardless of the relative sizes of the probe and the damage. In

contrast, the magnitude of the response depends both on the depth and on the relative sizes of the probe and the damage. It is quite probable that once the depth of the damage had been determined from the phase angle and the planar extent from the C-scan, the magnitude of the defect response could provide information on the through-thickness extent of the damaged region.

DISCUSSION

Experimental results indicated that the normalized impedance diagrams for all ferrite cup core probes are the same. In contrast to air core probes, the shapes of the cup core probes were observed to be independent of the number and distribution of the turns and of the wire size (except where there were frequency dependent shielding effects.) The shape was also observed to be independent of the resistivity of the test material and of the magnetic permeability of the ferrite, above some undetermined minimum. In addition, both the resistivity and depth models are simple and also independent of the probe and material properties mentioned above.

Accurate numerical solution of Maxwell's equations for the boundary conditions of a ferrite cup core probe with arbitrary permeability and in proximity to an arbitrary conductor appear to be difficult. The observations mentioned above, however, indicate that an approach that would extract the parametric variations of the measured quantities, such as the dependence of the change in coil impedance on material resistivity and defect depth may be more straight forward than previously expected.

The situation is simplified if one remembers that impedance values are normalized with respect to the air value, so it is only the variation of the impedance with respect to the sample properties that is treated. It is not the variation of the field map of the probe from the ideal that is significant, but rather its modification by the test material.³⁴

SUMMARY

The object of NDI is always the detection of defects or material abnormalities and, if possible, the quantitative measurement of those abnormalities. Abnormalities in graphite epoxy are generally of two types: fabrication-related and service-related. The former include weak interlaminar bonding, misplaced or twisted fibers, and porosity. Service-related abnormalities include delamination and broken fibers. Since eddy currents are carried by the graphite fibers, the method is sensitive to variations in fiber density and to broken fibers. Porosity is a characteristic of the nonconducting matrix and so is not detectable by eddy current. However, the same fabrication problems which cause the porosity may also cause a diminution in fiber density in the porous region and this lower fiber density would be detected. Since eddy current technology is ideally suitable to the in-service inspection environment and since the adversities suffered by the material during service usually result in broken fibers as well as delamination, the detection and measurement of broken fiber damage were identified as the goals of the project.

The very high resistivity of the material as well as its occasional frequency dependence were two technical issues to be addressed. A third was the geometrically irregular nature of the damage.

The high resistivity required the use of much larger probes than are standard in the eddy current inspection of metals. At the same time, the high resistivity permits the inspection of thicker material (up to several inches) than is usually associated with eddy current NDI. The nature of the damage required that the planar extent of the damage be determined. This was accomplished by generating a C-scan of the damage. The probe was raster-scanned across the surface and the associated change in a component of the impedance was used to generate a map of the detected damage. Accurate mapping requires the use of the smallest possible probe. Optimum resolution of the two conflicting requirements of a large probe to "see" the material and to provide adequate depth resolution and a small probe to generate an accurate C-scan required the development of a criterion by which to compare the effectiveness or sensitivity of different probes. The coupling coefficient of the probe was selected as the measure of the quality of the probe.

Based on this criterion, ferrite cup core probes were identified as the most effective of the possible surface or pancake variety of probes that are required for the single-sided inspection of flat components.³² The positive effects on probe sensitivity of both intrinsic and imposed shielding were determined.

The variation of resistivity among apparently similar materials and the dependence of resistivity on frequency required the development of a model or algorithm to calculate resistivity from the responses of ferrite cup core probes. The model estimated the resistivity of metals and a carbon/carbon composite to within at least $\pm 10\%$. The resistivities covered more than two orders of magnitude, ranging from $4 \mu\Omega\text{cm}$ to $842 \mu\Omega\text{cm}$. If the resistivity is known, the model provides an estimate of the thickness of the material. The model is independent of lift-off effects. Application of the model to graphite epoxy required that the geometric quantities (probe radius and material thickness) be multiplied by $\sqrt{2}$. The requirement for the use of this factor was attributed either to the complex conduction mechanisms in this type of composite material or to a requirement for additional factors in the model to address all high resistivity materials.

A second model was developed to measure the thickness of the undamaged material between the scanned surface and the damaged region. This model was accurate to within $\pm 10\%$. Errors were attributed to differences in lift-off separation at the point where the "good" material measurements were made and the point where the defect measurement was made, as well as to errors in resistivity measurements where they were required.

In conclusion, it appears it would be possible to design a ferrite cup core probe to inspect graphite epoxy components up to at least 5 inches (12.7 cm) thick if both surfaces were accessible. The broken-fiber damage can be mapped with a spatial resolution dependent on the size of the probe, and consequently on the thickness of the component. The thickness of the undamaged material between the scanned surface and the damage can be estimated.

REFERENCES

1. Cantwell, W.S., and Morton, S., "Detection of Impact Damage in CFRP Laminates," Composite Structures, 3, 1985, pp. 241-257.
2. Button, G.M., and Labor, J.D., Depot Level Repare for Compositse Structures: Development and Validation, Report No. NADC-79172-60, Volume 2, Mar 1985.
3. Phelps, M.L., In-Service Inspection Methods for Graphite-Epoxy Structures on Commercial Transport Aircraft, NASA-CR-165746, Final Report, Boeing Commercial Airplane Co., Seattle, Washington, Oct 1981.
4. Bar-Cohen, Y., and Crane, A.L., "Acoustic-Backscattering Imaging of Subcritical Flaws in Composites," Materials Evaluation, Aug 1982, pp. 970-975.
5. Dingwell, P.F., Mead, L.D. Nondestructive Inspection and Volume Fraction Determination Using an Eddy Current Method, Royal Aircraft Establishment, Farnborough (UK) RAE TR 76078, Jun 1976.
6. Owston, C.N., "Carbon Fibre Reinforced Polymers and Non-Destructive Testing," British Journal of NDT Vol. 15, No. 6, Jan 1973, pp. 2-11.
7. Prakash, R., and Owston, C.N., "Eddy-current Method for the Determination of Lay-up Order in Cross-plyed Crip Laminates," Composites, Vol. 7, No. 2, Apr 1976, pp. 88-92.
8. Owston, C.N., "Eddy Current Methods for the Examination of Carbon Fibre Reinforced Epoxy Resins," Materials Evaluation, Nov 1976, pp. 237-250.
9. Prakash, R., "Non-Destructive Testing of Composites," Composites, Oct 1980, pp. 217-224.
10. Lowney, J.R., and Goff, J.F. Fracture in Carbon--Epoxy Composites, NSWC/WO TR 77-179, 30 Sep 1977.
11. Howard, D.A., "The Effects of Subsurface Defects in Gr/E and Metal Matrix Composites," Proceedings of the Fourteenth Symposium on Nondestructive Evaluation, Ed. Moore, D.W. and Matzkanin, G.A. Southwest Research Institute, San Antonio, TX, 1984, pp. 299-312.
13. Dodd, C.V., Oak Ridge National Laboratory, Oak Ridge, TN, telephone conversation with S.N. Vernon, Naval Surface Warfare Center, Silver Spring, MD, concerning the resistivity of carbon/carbon and graphite epoxy samples, Jun 1985.
12. Allen, J.L., et. al, Electromagnetic Properties and Effects of Advanced Composite Materials: Measurement and Modeling, RADC-TRF-78-156, Jun 1987.

REFERENCES (Cont.)

14. Libby, Hugo L., Introduction to Electromagnetic Nondestructive Test Methods, Wiley-Interscience, New York, 1971.
15. McIntire, Paul, and Mester, Michael L., Eds., Nondestructive Testing Handbook, Second Edition, Vol. 4, Electromagnetic Testing, American Society for Nondestructive Testing, Inc., 1986.
16. Dodd, C.V., et.al., "Optimizing Defect Detection in Eddy Current Testing," Materials Evaluation, Mar 1971, pp. 59-62.
17. Vernon, S.N. and Gammell, P.M., "Optimization of Eddy Current Probes for the NDE of Carbon Fiber Composites," Proceedings of the Fifteenth Symposium on Non-Destructive Evaluation, Ed. Moore, D.W. and Matzkanin, G.A., Southwest Research Institute, San Antonio, TX, 1986, pp. 287-291.
18. Vernon, S.N., "Probe Properties Affecting the Eddy Current NDI of Graphite Epoxy," Review of Progress in Quantitative Non-Destructive Evaluation, Vol. 5B Ed. Thompson, D.O. and Chimenti, D.E., New York: Plenum Press, 1986, pp. 1113-1123.
19. Dodd, C.V., "The Use of Computer Modeling for Eddy Current Testing," Research Techniques in Nondestructive Testing, Volume III, Ed. Sharpe, R.S., New York: Academic Press, 1977.
20. Lord, W., "An Overview of Numerical Models for Eddy Current NDT Phenomena," Review of Progress in Quantitative Nondestructive Evaluation, Vol.6, Ed. Thompson D.O. and Chimenti, D.E. New York: Plenum Press, 1987.
21. Sabbagh, H.A., and Vernon, S.N., "Description and Verification of a Model of Eddy Current Probes with Ferrite Cores," Review of Progress in Quantitative Non-Destructive Evaluation, Vol. 34, Ed. Thompson, D.O., and Chimenti, D.E., New York: Plenum Press, 1984, pp. 653-662
22. Smith, S.H. and Dodd, C.V., "Optimization of Eddy Current Measurements," Materials Evaluation, Dec 1975, pp 279-283.
23. Vernon, S.N., and Gross, T.A.O., "Effects of Shielding on Properties of Eddy Current Probes with Ferrite Cup Coves," Review of Progress in Quantitative Non-Destructive Evaluation, Vol. 6, Ed. Thompson, D.O., and Chimenti, D.E., New York: Plenum Press, 1987.
24. Gross, T.A.O., Eddy Current Inspection of Graphite Epoxy Composites: Final Report, Naval Surface Weapons Center Contract No. N60921-85-C-0257, 7 Apr 1986.
25. Capobianco, T.E., "Field Mapping and Performance Characterization of Commercial Eddy Current Probes," Review of Progress in Quantitative Nondestructive Evaluation, Ed. Thompson, D.O., and Chimenti, D.E., New York: Plenum Press, 1987.
26. Burkhardt, G.L. and Fisher, S.L., "Eddy Current Probe Performance Variability," Review of Progress in Quantitative Nondestructive Evaluation, Ed. Thompson, D.O., and Chimenti, D.E., New York: Plenum Press, 1987.

REFERENCES (Cont.)

27. Dodd, C.V., et. al., "Analysis of Eddy Current Problems With a Time-Sharing Computer," Materials Evaluation, Vol. 27, No. 7, Jul 1969, pp 165-168.
28. Dodd, C.V. and Deeds, W.E., "Absolute Eddy Current Measurements of Electrical Conductivity," Review of Progress in Quantitative Nondestructive Evaluation, Vol.2, Ed. Thompson, D.O, and Chimenti, D.E., New York: Plenum Publishing Corp., 1982, pp 387-393.
29. Kahn, A.H., National Bureau of Standards, Gaithersburg, MD., letter to S.N. Vernon, Naval Surface Warfare Center, Silver Spring, MD, concerning the derivation of the normalized impedance for the one-dimensional eddy current case, Jun, 1986.
- 30 Warren, J.W., Vernon, S.N., and Gammell, P.M., "Ultrasonic and Eddy Current Inspection of a Thick Wall Graphite Epoxy Cylinder," Proceedings of the Sixteenth Symposium on Nondestructive Evaluation, Ed. Moore, D.W., and Matzkanin, G.A., Nondestructive Evaluation Testing Information Analysis Center, Southwest Research Institute, San Antonio, Texas, 1987.
31. Bailey, D. and McEleney, P., "Reference Standards for Electromagnetic Testing," Nondestructive Testing Handbook, Second Edition, Vol. 4, Electromagnetic Testing, Ed. McIntire, P., and Mester, M.L., American Society for Nondestructive Testing, Inc., 1986, pp. 252-264.
32. Freeman, S.M., Characterization of Lamina and Interlaminar Damage in Graphite-Epoxy Laminates by the Depty Technique, ASTM-STP 757, 1987, pp. 50-62.
33. Jamison, R.D., "Fiber Fraction in Composite Laminates," Proceedings of the ICCM VI, Held at Imperial College, London, England, 20-25 Jul 1987.
34. Ida, N., "Eddy Current Transducers," Nondestructive Testing Handbook, Second Edition, Vol.4, Electromagnetic Testing, Ed. P. McIntire and M.L. Mester, American Society for Nondestructive Testing, Inc., 1986, pp 53-68.

NOMENCLATURE

α	Compliment of θ_L
β	Angle related to thickness effect
δ	Skin depth
μ	Magnetic permeability
ρ	Electrical resistivity ($\mu\Omega\text{cm}$)
σ	Electrical conductivity
θ_D	Defect response phase angle
θ_L	Lift-off angle
θ_N	Normalized defect response phase angle
ω	Angular frequency = $2\pi f$
a	Defect depth, distance between scanned surface and defect.
f	Frequency (Hertz)
r	Mean core radius = $1/3$ outside diameter
R_o	Resistive component of probe impedance in air (ohm)
R_m	Resistive component of probe impedance when coupled to test material (ohm)
R_n	Normalized resistive component = $(R_m - R_o)/X_o$
X_o	Reactive component of probe impedance in air (ohm)
X_c	Normalized reactive component as conductivity and/or frequency approach infinity
X_m	Reactive component when probe is coupled to test material (ohm)
X_n	Normalized reactive component = X_m/X_o

APPENDIX A

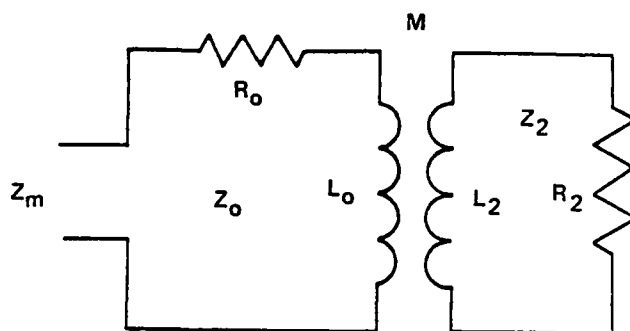
DERIVATION OF RELATIONSHIP BETWEEN THE COUPLING COEFFICIENT AND X_c 

FIGURE A-1. COUPLED CIRCUIT DIAGRAM

An eddy current probe and the test material can be compared to two coupled circuits (Figure A-1) where the primary, #0, represents the probe, and the secondary circuit, #2, represents the test material.

Z_m is the impedance measured when the two circuits are coupled.

$$Z_m = Z_0 + \frac{M^2}{Z_2} \quad \text{according to principles of electronics where } M \text{ is the mutual inductance given by}$$

$$M = K\sqrt{L_0 L_2}.$$

$$Z_2 = R_2 + i\omega L_2 \quad \text{and} \quad Z_0 = R_0 + i\omega L_0, \quad \text{so}$$

$$Z_m = R_0 + i\omega L_0 + \frac{\omega^2 K^2 L_0 L_2}{R_2 + i\omega L_2}$$

We are interested in X_c , the point where the impedance curve intercepts the ordinate axis having been extrapolated to high conductivity (or frequency), so $R_2 = 0$. Consequently,

$$Z_m = R_0 + i\omega L_0(1-K^2).$$

Therefore at the intercept point where the conductivity approaches infinity the normalized imaginary component of the impedance, X_c , is given by

$$X_c = \frac{i\omega L_0(1-K^2)}{i\omega L_0} = (1-K^2) \text{ or } K^2 = 1 - X_c$$

APPENDIX B

ONE-DIMENSIONAL EDDY CURRENT CASE

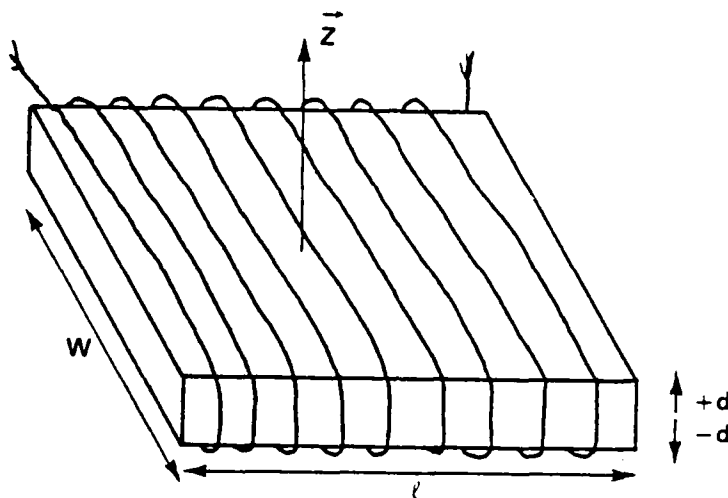


FIGURE B-1. ONE-DIMENSIONAL FIELD

Consider a conducting slab (Figure B-1) which is subjected to a uniform magnetic field that varies only in the Z-direction, the direction normal to the slab.

Neglecting end effects, the field in the slab is

$$H = H_0 \frac{\cos kz}{\cos kd}$$

where $k = \frac{1+i}{\delta}$ and $i = \sqrt{-1}$. This is the solution of $(\nabla^2 + k^2)H = 0$ and satisfies the boundary conditions of $H = H_0$ at $z = \pm d$.

$$E = \frac{1}{\sigma} \nabla \times H,$$

$$E = \frac{1}{\sigma} \begin{vmatrix} \hat{i} & \hat{j} & \hat{k} \\ \partial_x & \partial_y & \partial_z \\ 0 & H_y & 0 \end{vmatrix},$$

$$E = -\frac{1}{\sigma} i \frac{\partial H}{\partial z} = \frac{1}{\sigma} \frac{\partial H}{\partial z} i,$$

$$E = E_x = -\frac{1}{\sigma} \frac{\partial}{\partial z} H_0 \frac{\cos kz}{\cos kd} = \frac{1}{\sigma} H_0 k \frac{\sin kz}{\cos kz}.$$

At the surface,

$$E(d) = \frac{H_0}{\sigma} k \tan kd.$$

Integrating the Poynting vector ($\frac{1}{2} E_x H^*$) over the surface of the slab, neglecting end effects and time averaging gives

$$\int \frac{1}{2} E_x H^* ds = -\frac{1}{2} |H_0|^2 \frac{k \tan kd}{\sigma} \times 2wl$$

where $E_x H^*$ is the component on the inward normal, pointing into the surface, and $2wl$ is the area of the two surfaces.

The power through the area ds is given by

$$\int \frac{1}{2} E_x H^* ds = \frac{1}{2} I^* V = \frac{1}{2} I^* IZ$$

where Z is the impedance seen by the current source. According to Ampere's Law, $H_0 = n' I_0$, where n' is the number of turns per unit length. Therefore,

$$Z = -(n')^2 \frac{k \tan kd}{\sigma} 2wl$$

$$\lim_{k \rightarrow 0} Z = -(n')^2 \frac{k^2 d}{\sigma} \times 2wl$$

Since $k = \frac{1+i}{\delta}$ and $\delta^2 = 2/\omega\sigma\mu_0$,

$$\lim_{k \rightarrow 0} Z = -i(n')^2 \omega\mu_0 (2dl).$$

$$\lim_{k \rightarrow \infty} \tan kd = \frac{e^{ikd} - e^{-ikd}}{i(e^{ikd} + e^{-ikd})} = \frac{-e^{ikd}}{-e^{-ikd}} = i.$$

Therefore,

$$\lim_{k \rightarrow \infty} Z = -(n')^2 \frac{ki}{\sigma} 2wl,$$

$$\lim_{k \rightarrow \infty} Z = -(n')^2 \frac{(i+1)i}{\sigma\delta} (2wl), \text{ and}$$

$$\lim_{k \rightarrow \infty} Z = (n')^2 \frac{(i-1)}{\sigma \delta} (2wl).$$

To normalize the impedance of the coil with respect to the coil impedance in the absence of the slab, we divide by

$$\omega L_0 = (n')^2 \omega \mu_0 2dw l$$

The normalized impedance, Z_n , is given by

$$Z_n = \frac{-(n')^2 k \tan kd \, 2wl}{\sigma (n')^2 \omega \mu_0 2dw l},$$

$$Z_n = \frac{ik \tan kd}{i\sigma \omega d},$$

$$Z_n = \frac{ik \tan kd}{k^2 d},$$

$$Z_n = \frac{i \tan kd}{kd}.$$

Since $k = \frac{1+i}{\delta}$,

$$Z_n = \frac{-i}{kd} \left[\frac{\sin \frac{2d}{\delta} + i \sinh \frac{2d}{\delta}}{\sin \frac{2d}{\delta} + i \cosh \frac{2d}{\delta}} \right]$$

$$Z_n = -\frac{1}{\frac{2d}{\delta}} \left[\frac{(\sin \frac{2d}{\delta} - \sinh \frac{2d}{\delta}) + i(\sin \frac{2d}{\delta} + \sinh \frac{2d}{\delta})}{\cos \frac{2d}{\delta} + \cosh \frac{2d}{\delta}} \right]$$

The real component of this normalized impedance is given by

$$R_n = \frac{-\delta}{2d} \frac{\sin \frac{2d}{\delta} - \sinh \frac{2d}{\delta}}{\cos \frac{2d}{\delta} + \cosh \frac{2d}{\delta}},$$

and the imaginary component is given by

$$X_n = -\frac{\delta}{2d} \frac{\left[\sin \frac{2d}{\delta} + \sinh \frac{2d}{\delta_i} \right]}{\left[\cos \frac{2d}{\delta} + \cosh \frac{2d}{\delta_i} \right]}$$

The tangent of the lift-off angle, θ_L , is given by

$$\tan \theta_L = \frac{1 - X_n}{R_n} \quad (B-1)$$

where \underline{d} is taken to be the equivalent of the mean coil radius .

Values of r/δ were substituted in equation B-1 to obtain the data shown in Figure 15.

DISTRIBUTION

	Copies		Copies
Office of Chief of Naval Research		Department of the Navy	
Office of Naval Technology		Naval Air Systems Command	
Attn: J. Kelly, OCNR222	1	Attn: AIR 5304B1	1
Washington, D.C. 20360		Washington, D.C. 20361-5300	
Department of the Navy		Naval Aviation Depot	
Strategic Systems Project Office		Attn: Robert Mathus, Code 34133	1
Attn: B.W. Hannah, Code SP272	1	U.S. NAS, North Island	
Crystal Mall No. 3		San Diego, CA 92135	
Washington, D.C.		Naval Aviation Depot	
Naval Air Systems Command		Materials Engineering Division	
Attn: Steve Stephenson	1	Attn: Carl Singleton, Code 34100	1
1421 Jefferson Davis Highway		U.S. NAS Pensacola, FL 32508	
Washington, D.C. 20361		Naval Aviation Depot	
David W. Taylor Naval Ship Research Center		Attn: Tom Robertshaw EDSO 341	1
Attn: I. Caplan, Code 012.5	1	Martin Rossen EDSO 341	1
Robert DeNale, Code 2815	1	U.S. NAS	
Annapolis Laboratory		Alameda, CA 94501	
Annapolis, MD 21402		Naval Aviation Depot	
Naval Air Development Center		Attn: John Lundeen, Code 341	1
Attn: Gwynn McConnell, Code 6063	1	U.S. NAS	
Warminster, PA 18974		Jacksonville, FL 32212-0016	
Naval Research Laboratory		U.S. Naval Academy	
Attn: H. Chaskelis, Code 5834	1	Attn: Prof. Olaf Rask	1
Washington, D.C. 20375		Systems Engineering Dept.	
Naval Aviation Depot		Annapolis, MD 21402	
Attn: Ken Fizer, Code 36050	1	NICAS	
U.S. NAS		Attn: Jack O'Rourke, Code 35410	1
Norfolk, VA 23511		Cherry Point, NC 28533-5030	

DISTRIBUTION (Cont.)

	Copies		Copies
Department of the Army Attn: Donald R. Artis ODCSRDA/DAMA/ART Room 3E429, Pentagon Washington, D.C. 20310-0633	1	National Bureau of Standards Attn: Dr. Leonard Mordfin Dr. Arnold Kahn Gaithersburg, MD 20899	1 1
Department of the Army Materials Technology Laboratory Attn: SLCMT, Dr. A.L. Broz Watertown, MA 02172	1	National Bureau of Standards Attn: Tom Capobianco, Code 724.05 325 Broadway Boulder, CO 80303	1
U.S. Army Research Office Attn: Dr. George Mayer Director of Materials Science Research Triangle Park, N.C. 27709	1	Oak Ridge National Laboratory Attn: Dr. C.V. Dodd P.O. Box X Oak Ridge, TN 37830	1
Army Materials Technology Laboratory Attn: SLCMT-MEF (P.C. McEleney) SLCMT-MRM (D.J. Strand) Watertown, MA 02172	1 1	Defense Technical Information Center Cameron Station, VA 22314	12
USAF AFWAL Materials Laboratory Attn: Donald M. Forney Wright-Patterson AFB, OH 45433	1	Library of Congress Attn: Gift & Exchange Division Washington, D.C. 20540	4
SA-ALC/MMEI Attn: Maj. David Jirele Kelly AFB, TX 78241	3	American Research Corp. of Va. Attn: Howard Groger P.O. Box 3406 Radford, VA 24143-3406	1
SM-ALC/MAQCA Attn: Donald M. Bailey McClellan AFB, CA 93652-5000	1	Southwest Research Institute Department of Research and Development Attn: Jay Fisher 6220 Culebra Road P.O. Drawer 28510 San Antonio, TX 78284	1
Defense Advanced Research Project Agency (DARPA) Attn: Dr. Ben A. Wilcox 1400 Wilson Boulevard Arlington, VA 22209	1	TAO Gross, Inc. Attn: T.A.O. Gross 230 Concord Road Lincoln, MD 01773-4116	1
NASA/Lewis Research Center Attn: Dr. Stan Kilma 21000 Brookpark Road Cleveland, OH 44135	1	Martin Marietta Laboratories Attn: Dr. Boro Djordjevic 1450 South Rolling Road Baltimore, MD 21227	1

DISTRIBUTION (Cont.)

Copies

Martin Marietta Aerospace
Attn: Gerald W. Scott 1
Advanced Quality Technology
P.O. Box 29304
New Orleans, LA 70189

Hercules Aerospace Company
Attn: W.J. Murri 1
Aerospace Products Group
P.O. Box 30181
Salt Lake City, UT 84130-0181

LTV Aerospace and Defense Co.
Attn: Anthony B. Hamilton 1
P.O. Box 225907
Dallas, TX 75265

McDonald-Douglas
Attn: Longin Greszczuk, MS 13/C 1
Huntington Beach, CA 92647

Martin Marietta Aerospace
Attn: Ward Rummel 1
Denver Aerospace
P.O. Box 179, MS 0626
Denver CO 80201

The Johns Hopkins University
Attn: Dr. Robert E. Green, Jr. 1
Materials Science & Engineering
MD Hall 102
Baltimore, MD 21218

Internal Distribution
E231 2
E232 15
E35 (GIDIP Office) 1
D211 (Ramsey D. Johnson) 5
R30 1
R34 1
R34 (S. Vernon) 20
C72W 1

END

DATE

FILMED

APRIL

1988

DTIC